What Are Bayesian Neural Network Posteriors Really Like?

Pavel Izmailov New York University
Sharad Vikram Google Research
Matthew D. Hoffman Google Research
Andrew Gordon Wilson New York University

Abstract

The posterior over Bayesian neural network (BNN) parameters is extremely high-dimensional and non-convex. For computational reasons, researchers approximate this posterior using inexpensive mini-batch methods such as mean-field variational inference or stochastic-gradient Markov chain Monte Carlo (SGMCMC). To investigate foundational questions in Bayesian deep learning, we instead use full-batch Hamiltonian Monte Carlo (HMC) on modern architectures. We show that (1) BNNs can achieve significant performance gains over standard training and deep ensembles; (2) a single long HMC chain can provide a comparable representation of the posterior to multiple shorter chains; (3) in contrast to recent studies, we find posterior tempering is not needed for near-optimal performance, with little evidence for a "cold posterior" effect, which we show is largely an artifact of data augmentation; (4) BMA performance is robust to the choice of prior scale, and relatively similar for diagonal Gaussian, mixture of Gaussian, and logistic priors; (5) Bayesian neural networks show surprisingly poor generalization under domain shift; (6) while cheaper alternatives such as deep ensembles and SGMCMC can provide good generalization, they provide distinct predictive distributions from HMC. Notably, deep ensemble predictive distributions are similarly close to HMC as standard SGLD, and closer than standard variational inference.

1. Introduction

Over the last 25 years, there have been several strong arguments favouring a Bayesian approach to deep learning (e.g., MacKay, 1995; Neal, 1996; Blundell et al., 2015; Gal, 2016; Wilson & Izmailov, 2020). Bayesian inference for neural networks promises improved predictions, reliable uncertainty estimates, and principled model comparison, naturally supporting active learning, continual learning, and decision-making under uncertainty. The Bayesian deep learning community has designed multiple successful practical methods inspired by the Bayesian approach (Blundell et al., 2015; Gal & Ghahramani, 2016; Welling & Teh, 2011; Kirkpatrick et al., 2017; Maddox et al., 2019; Izmailov et al., 2019; Daxberger et al., 2020) with applications ranging from astrophysics (Cranmer et al., 2021) to automatic diagnosis of Diabetic Retinopathy (Filos et al., 2019), click-through rate prediction in advertising (Liu et al., 2017) and modeling of fluid dynamics (Geneva & Zabaras, 2020).

However, inference with modern neural networks is distinctly challenging. We wish to compute a Bayesian model average corresponding to an integral over a multi-million dimensional multi-modal posterior, with unusual topological properties like mode-connectivity (Garipov et al., 2018; Draxler et al., 2018), under severe computational constraints.

There are therefore many unresolved questions about Bayesian deep learning practice. Variational procedures typically provide unimodal Gaussian approximations to the multimodal posterior. Practically successful methods such as deep ensembles (Lakshminarayanan et al., 2017; Fort et al., 2019) have a natural Bayesian interpretation (Wilson & Izmailov, 2020), but only represent modes of the posterior. While Stochastic MCMC (Welling & Teh, 2011; Chen et al., 2014; Zhang et al., 2020b) is computationally convenient, it could be providing heavily biased estimates of posterior expectations. Moreover, Wenzel et al. (2020) question the quality of standard Bayes posteriors, citing results where "cold posteriors", raised to a power $1/T$ with $T < 1$, improve performance.

Additionally, Bayesian deep learning methods are typically evaluated on their ability to generate useful, well-calibrated predictions on held-out or out-of-distribution data. However, strong performance on benchmark problems does not imply that the algorithm accurately approximates the true Bayesian model average (BMA).

In this paper, we investigate fundamental open questions in Bayesian deep learning, using multi-chain full-batch Hamiltonian Monte Carlo (HMC, Neal et al., 2011). HMC is a highly-efficient and well-studied Markov Chain Monte Carlo (MCMC) method that is guaranteed to asymptotically produce samples from the true posterior. However it is

enormously challenging to apply HMC to modern neural networks due to its extreme computational requirements: HMC can take *tens of thousands of training epochs* to produce a single sample from the posterior. To address this computational challenge, we parallelize the computation over hundreds of Tensor processing unit (TPU) devices.

We argue that full-batch HMC provides the most precise tool for studying the BNN posterior to date. We are not proposing HMC as a computationally efficient method for practical applications. Rather, using our implementation of HMC we are able to explore fundamental questions about posterior geometry, the performance of BNNs, approximate inference, effect of priors and posterior temperature.

In particular, we show: (1) BNNs can achieve significant performance gains over standard training and deep ensembles; (2) a single long HMC chain can provide a comparable representation of the posterior to multiple shorter chains; (3) in contrast to recent studies, we find posterior tempering is not needed for near-optimal performance, with little evidence for a "cold posterior" effect, which we show is largely an artifact of data augmentation; (4) BMA performance is robust to the choice of prior scale, and relatively similar for diagonal Gaussian, mixture of Gaussian, and logistic priors over weights. This result highlights the importance of architecture relative to parameter priors in specifying the prior over functions. (5) While Bayesian neural networks have good performance for OOD detection, they show surprisingly poor generalization under domain shift; (6) while cheaper alternatives such as deep ensembles and SGMCMC can provide good generalization, they provide distinct predictive distributions from HMC. Notably, deep ensemble predictive distributions are similarly close to HMC as standard SGLD, and closer than standard variational inference.

We additionally show how to effectively deploy full batch HMC on modern neural networks, including insights about how to tune crucial hyperparameters for good performance, and parallelize sampling over hundreds of TPUs. Our HMC samples and implementation will be a public resource. We hope this resource will both serve as a reference in evaluating and calibrating more practical alternatives to HMC, and aid in exploring questions for a better understanding of approximate inference in Bayesian deep learning.

2. Background

Bayesian neural networks The goal of classical learning is to find a single best setting of the parameters for the model, typically through maximum-likelihood optimization. In the Bayesian framework, the learner instead infers a *posterior* distribution $p(w|\mathcal{D})$ over the parameters w of the model after observing the data $\mathcal{D}$. The posterior distribution is given by Bayes' rule: $p(w|\mathcal{D}) \propto p(\mathcal{D}|w)p(w)$, where $p(\mathcal{D}|w)$ is the likelihood of $\mathcal{D}$ given by the model with parameters w, and $p(w)$ is the prior distribution over the parameters. The predictions of the model on a new test example x are then given by the *Bayesian model average* (BMA)

$$p(y|x, \mathcal{D}) = \int_w p(y|x, w)p(w|\mathcal{D})dw, \tag{1}$$

where $p(y|x, w)$ is the predictive distribution for a given value of the parameters w. This BMA is particularly compelling in Bayesian deep learning, because the posterior over parameters for a modern neural network can represent many complementary solutions to a given problem, corresponding to different settings of parameters (Wilson & Izmailov, 2020). Unfortunately, the integral in Eq. (1) cannot be evaluated in closed form for neural networks, so one must resort to approximate inference. Moreover, approximating Eq. (1) is challenging due to a high dimensional and sophisticated posterior $p(w|\mathcal{D})$. For a detailed discussion of Bayesian deep learning, see e.g. Wilson & Izmailov (2020).

Markov Chain Monte Carlo. The integral in Eq. (1) can be approximated by sampling: $p(y|x, \mathcal{D}) \approx \frac{1}{M}\sum_{i=1}^{M} p(y|x, w_i)$, where $w_i \sim p(w|\mathcal{D})$ are samples drawn from the posterior. MCMC methods construct a Markov chain that, if simulated for long enough, generates approximate samples from the posterior. In this work, we focus on Hamiltonian Monte Carlo (Neal et al., 2011), a method that produces asymptotically exact samples assuming access to the unnormalized posterior density $p(\mathcal{D}|w)p(w)$ and its gradient.

3. Related work

The bulk of work on Bayesian deep learning has focused on scalable approximate inference methods. These methods include stochastic variational inference (Hoffman et al., 2013; Graves, 2011; Blundell et al., 2015; Kingma et al., 2015; Molchanov et al., 2017; Louizos & Welling, 2017; Khan et al., 2018; Zhang et al., 2018; Wu et al., 2018; Osawa et al., 2019; Dusenberry et al., 2020), dropout (Srivastava et al., 2014; Gal & Ghahramani, 2016; Kendall & Gal, 2017; Gal et al., 2017), the Laplace approximation (MacKay, 1992; Kirkpatrick et al., 2017; Ritter et al., 2018; Li, 2000; Daxberger et al., 2020), expectation propagation (Hernández-Lobato & Adams, 2015), and leveraging the stochastic gradient descent (SGD) trajectory, either for a deterministic approximation, or sampling as in SGLD (Mandt et al., 2017; Maddox et al., 2019; Izmailov et al., 2018; Wilson & Izmailov, 2020). Foong et al. (2019) and Farquhar et al. (2020) additionally consider the role of expressive posterior approximations in variational inference.

While these (and many other) methods often provide improved predictions or uncertainty estimates, to the best of our knowledge *none* of these methods have been directly

evaluated on their ability to match the true posterior distribution using practical architectures and datasets. Moreover, many of these methods are often designed with train-time constraints in mind, to take roughly the same amount of compute as regular SGD training. To evaluate approximate inference procedures, and explore fundamental questions in Bayesian deep learning, we attempt to construct a posterior approximation of the highest possible quality, ignoring the practicality of the method.

The Monte Carlo literature for Bayesian neural networks has mainly focused on stochastic gradient-based methods (Welling & Teh, 2011; Ahn et al., 2014; Chen et al., 2014; Ma et al., 2015; Ahn et al., 2012; Ding et al., 2014; Zhang et al., 2020b; Garriga-Alonso & Fortuin, 2021) for computational efficiency reasons. These methods are fundamentally biased: (1) they omit the Metropolis-Hastings correction step, and (2) the noise from subsampling the data perturbs their stationary distribution. In particular, Betancourt (2015) argues that HMC is incompatible with data subsampling. Notably, Zhang et al. (2020a) recently proposed a second-order stochastic gradient MCMC method that is asymptotically exact.

Since the classic work of Neal (1996), there have been a few recent attempts at using full-batch HMC in BNNs (e.g.; Cobb & Jalaian, 2020; Wenzel et al., 2020). These studies tend to use relatively short trajectory lengths (generally not considering a number of leapfrog steps greater than 100), and tend to focus on relatively small datasets and networks. We on the other hand experiment with practical architectures and datasets and use up to 10^5 leapfrog steps per iteration to ensure good mixing.

Our work is aimed at *understanding* the properties of true Bayesian neural networks. In a similar direction, Wenzel et al. (2020) have recently explored the effect of the posterior temperature in Bayesian neural networks. We discuss their results in detail in Section 7, and provide our own exploration of the posterior temperature with a different result: we find that BNNs achieve strong performance at temperature 1 and do not require posterior tempering. Moreover, the scope of our paper extends well beyond temperature scaling, revealing for instance that while BNNs can provide strong in-domain generalization, they surprisingly suffer on the covariate shift problems that approximate inference methods are often applied towards. We also show that while deep ensembles are often treated as a non-Bayesian alternative, they in fact are providing higher fidelity approximations of the Bayesian model average than standard approximate inference procedures, as argued in Wilson & Izmailov (2020). We also explore several other key questions, including prior selection and posterior geometry.

4. HMC for deep neural networks

We use full-batch Hamiltonian Monte Carlo (HMC) to sample from the parameter posteriors for Bayesian neural networks. In this section, we show how to make HMC effective for modern Bayesian neural networks, discussing important details such as hyper-parameter specification. In the next sections, we use the HMC samples to explore fundamental questions about approximate inference in modern deep learning. We summarize HMC in Appendix Algorithm 1 and Algorithm 2. Intuitively, HMC is simulating the dynamics of a particle sliding on the plot of the density function that we are trying to sample from.[1]

Implementation. To scale HMC to modern neural network architectures and for datasets like CIFAR-10 and IMDB, we parallelize the computation over 512 TPUv3 devices[2] (Jouppi et al., 2020). We execute HMC in a single-program multiple-data (SPMD) configuration, wherein a dataset is sharded evenly over each of the devices and an identical HMC implementation is run on each device. Each device maintains a synchronized copy of the Markov chain state, where the full-batch gradients needed for leapfrog integration are computed using cross-device collectives. We release our JAX (Bradbury et al., 2018) implementation.

Neural network architectures. In our evaluation, following Wenzel et al. (2020), we primarily focus on two architectures: ResNet-20-FRN and CNN-LSTM. ResNet-20-FRN is a residual architecture (He et al., 2016) of depth 20 with batch normalization layers (Ioffe & Szegedy, 2015) replaced with filter response normalization (FRN; Singh & Krishnan, 2020). Batch normalization makes the likelihood harder to interpret by creating dependencies between training examples, whereas the outputs of FRN layers are independent across inputs. We use Swish (SiLU) activations (Hendrycks & Gimpel, 2016; Elfwing et al., 2018; Ramachandran et al., 2017) instead of ReLUs to ensure smoothness of the posterior density surface, which we found improves acceptance rates of HMC proposals without hurting the overall performance. The CNN-LSTM is a long short-term memory network (Hochreiter & Schmidhuber, 1997) adapted from Wenzel et al. (2020) without modifications.

Datasets and Data Augmentation. In our main evaluations we use the CIFAR image classification datasets (Krizhevsky et al., 2014) and the IMDB dataset (Maas et al., 2011) for sentiment analysis. We do not use any data augmentation, both because the random augmentations introduce stochasticity into the evaluation of the posterior log-density and its gradient, and because the expected randomly

[1] For a detailed introduction to HMC please see Neal et al. (2011). See also interactive visualization here: `http://chi-feng.github.io/mcmc-demo/`.

[2] We use other hardware configurations in several experiments. We state the hardware that we used in the corresponding sections.

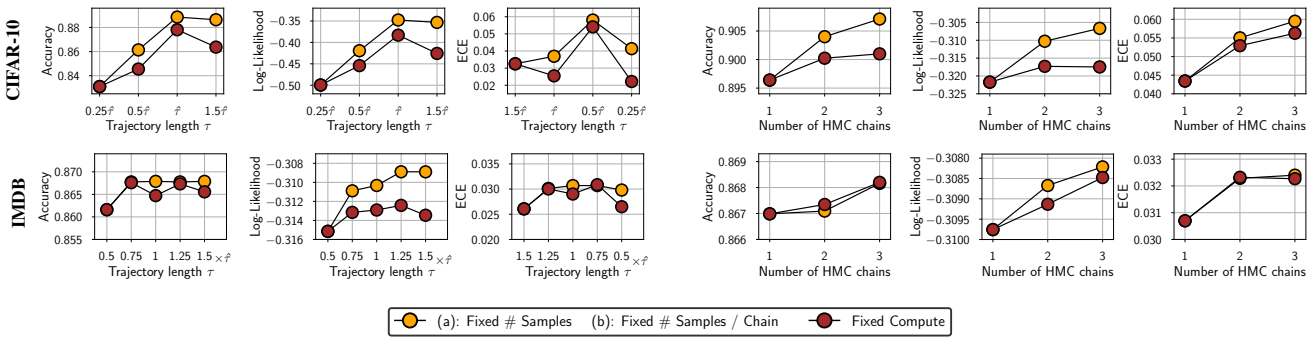

(a) Trajectory length ablation

(b) Number of chains ablation

Figure 1. **Effect of HMC hyper-parameters.** BMA accuracy, log-likelihood and expected calibration error (ECE) as a function of **(a)**: the trajectory length τ and **(b)**: number of HMC chains. The orange curve shows the results for a fixed number of samples in (a) and for a fixed number of samples per chain in (b); the brown curve shows the results for a fixed amount of compute. All experiments are done on CIFAR-10 using the ResNet-20-FRN architecture on IMDB using CNN-LSTM. Longer trajectory lengths decrease correlation between subsequent samples improving accuracy and log-likelihood. For a given amount of computation, increasing the number of chains from one to two modestly improves the accuracy and log-likelihood.

perturbed log-likelihood does not have a clean interpretation as a valid likelihood function (Wenzel et al., 2020). In this section we perform ablations using ResNet-20-FRN on CIFAR-10 and CNN-LSTM on IMDB.

4.1. Trajectory length τ

The trajectory length parameter τ determines the length of the dynamics simulation on each HMC iteration. Effectively, it determines the correlation of subsequent samples produced by HMC. To suppress random-walk behavior and speed up mixing, we want the length of the trajectory to be relatively high. But increasing the length of the trajectory also leads to an increased computational cost: the number of evaluations of the gradient of the target density (evaluations of the gradient of the loss on the full dataset) is equal to the ratio τ/Δ of the trajectory length to the step size.

We suggest the following value of the trajectory length τ:

$$\hat{\tau} = \frac{\pi \alpha_{\text{prior}}}{2}, \tag{2}$$

where α_{prior} is the standard deviation of the prior distribution over the parameters. If applied to a spherical Gaussian distribution, HMC with a small step size and this trajectory length will generate exact samples[3]. While we are interested in sampling from the posterior rather than from the spherical Gaussian prior, we argue that in large BNNs the prior tends to determine the scale of the posterior. We provide more detail and confirm this intuition empirically in the Appendix C.

In order to test the validity of our recommended trajectory length, we perform an ablation and report the results in Figure 1(a). As expected, longer trajectory lengths provide better performance in terms of accuracy and log-likelihood. Expected calibration error is generally low across the board. The trajectory length $\hat{\tau}$ provides good performance in all three metrics. This result confirms that, despite the expense, when applying HMC to BNNs it is actually helpful to use tens of thousands of gradient evaluations per iteration.

4.2. Step size Δ

The step size parameter Δ determines the discretization step size of the Hamiltonian dynamics and consequently the number of leapfrog integrator steps. Lower step sizes lead to a better approximation of the dynamics and higher rates of proposal acceptance at the Metropolis-Hastings correction step. However, lower step sizes require more gradient evaluations per iteration to hold the trajectory length τ constant.

Using ResNet-20-FRN on CIFAR-10, we run HMC for 50 iterations with step sizes of $1 \cdot 10^{-5}$, $5 \cdot 10^{-5}$, $1 \cdot 10^{-4}$, and $5 \cdot 10^{-4}$ respectively, ignoring the Metropolis-Hastings correction. We find the chains achieve average accept probabilities of 72.2%, 46.3%, 22.2%, and 12.5%, reflecting large drops in accept probability as step size is increased. We also observe BMA log-likelihoods of -0.331, -0.3406, -0.3407, and -0.895, indicating that higher accept rates result in higher likelihoods.

4.3. Number of HMC chains

We can improve the coverage of the posterior distribution by running multiple independent chains of HMC. Effectively, each chain is an independent run of the procedure using a different random initialization. Then, we combine the samples

[3]Since the Hamiltonian defines a set of independent harmonic oscillators with period $2\pi\alpha$, $\tau = \pi\alpha/2$ applies a quarter-turn in phase space, swapping the positions and momenta.

from the different chains. The computational requirements of running multiple chains are hence proportional to the number of chains.

We report the Bayesian model average performance as a function of the number of chains in Figure 1(b). Holding compute budget fixed, using two or three chains is only slightly better than using one chain. This result notably shows that HMC is relatively unobstructed by energy barriers in the posterior surface that would otherwise require multiple chains to overcome. We explore this result further in Section 5.

5. How well does HMC mix?

The primary goal of our paper is to construct accurate samples from the posterior, and use them to understand the properties of Bayesian neural networks better. In this section we consider several diagnostics to evaluate whether our HMC sampler has converged, and discuss their implications to the posterior geometry. We consider mixing in both *weight space* and *function space*. A distribution over weights w combined with a neural network architecture $f(x, w)$ induces a distribution over functions $f(x)$. Ultimately, since we are using functions to make predictions, we care mostly about mixing in function space.

Summary: HMC is able to mix surprisingly well in function space, and better than in parameter space. Geometrically, HMC is able to explore connected basins of the posterior with high functional diversity.

5.1. $\hat{R}$ diagnostics

We apply the classic Gelman et al. (1992) "$\hat{R}$" potential-scale-reduction diagnostic to our HMC runs. Given two or more chains, $\hat{R}$ estimates the ratio between the between-chain variance (i.e., the variance estimated by pooling samples from all chains) and the average within-chain variance (i.e., the variances estimated from each chain independently). The intuition is that, if the chains are stuck in isolated regions, then combining samples from multiple chains will yield greater diversity than taking samples from a single chain. For the precise mathematical definition of $\hat{R}$, please see the Appendix B.

We compute $\hat{R}$ using TensorFlow Probability's implementation[4] (Lao et al., 2020) for both the weights and the test-set softmax predictions on CIFAR-10 with ResNet-20-FRN and on IMDB with CNN-LSTM. We report the results in Figure 2. We observe that on both IMDB and CIFAR, the bulk of the function-space $\hat{R}$ values is concentrated near

[4] tfp.mcmc.potential_scale_reduction

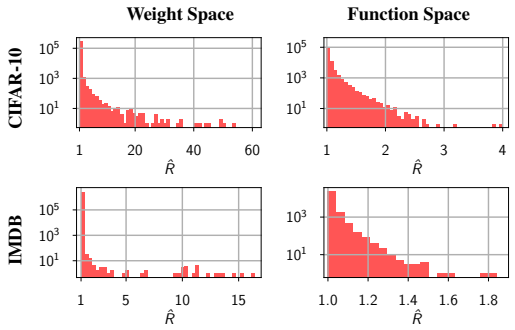

Figure 2. **Log-scale histograms of $\hat{R}$ convergence diagnostics.** Function-space $\hat{R}$s are computed on the test-set softmax predictions of the classifiers and weight-space $\hat{R}$s are computed on the raw weights. About 91% of CIFAR-10 and 98% of IMDB posterior-predictive probabilities get an $\hat{R}$ less than 1.1. Most weight-space $\hat{R}$ values are quite small, but enough parameters have very large $\hat{R}$s to make it clear that the chains are sampling from different distributions in weight space.

1, meaning intuitively that a single chain can capture the diversity of predictions on most of the test data points nearly as well as multiple chains. The mixing is especially good on the IMDB dataset, where only 2% of inputs correspond to $\hat{R}$ larger than 1.1. In Appendix E we apply HMC to a synthetic regression problem and show that HMC can indeed mix in the prediction space: different HMC chains provide very similar predictions.

In weight space, although most parameters show no evidence of poor mixing, some have very large $\hat{R}$s, indicating that there are directions in which the chains fail to mix.

Implications for the Posterior Geometry. The fact that a single HMC chain is able to mix well in function space (aka prediction space) suggests that the posterior contains connected regions which correspond to high functional diversity. Indeed, a single HMC chain is extremely unlikely to jump between isolated modes, but appears able to produce samples with diverse predictions. Moreover, HMC is able to navigate these regions effeciently. Prior work on *mode connectivity* (Garipov et al., 2018; Draxler et al., 2018) has shown that there exist paths of high density connecting different modes of the posterior. Our observations suggest a stronger version of mode connectivity: not only do mode-connecting paths exist between functionally diverse modes, but also at least some of these paths can be leveraged by Monte Carlo methods to efficiently explore the posterior.

5.2. Posterior density visualizations

To further investigate how HMC is able to explore the posterior over the weights, we visualize a cross-section of the posterior density in subspaces of the parameter space containing the samples. Following Garipov et al. (2018), we

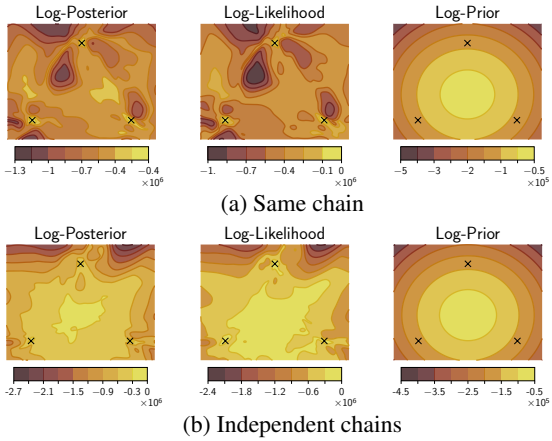

Figure 3. **Posterior density visualization.** Visualizations of posterior log-density, log-likelihood and log-prior in the two-dimensional subspace of the parameter space spanned by three HMC samples from **(a)** the same chain and **(b)** three independent chains. Each HMC chain explores a region of high posterior density of a complex non-convex shape, that appears multi-modal in the presented cross-sections.

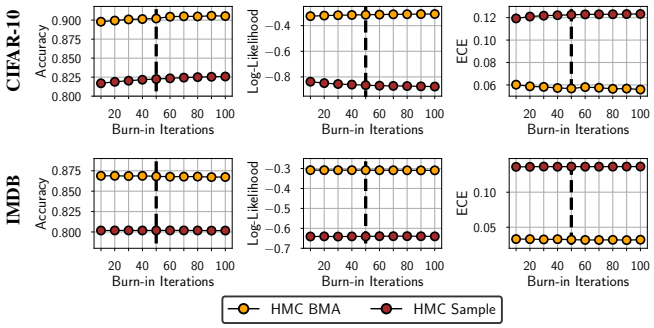

Figure 4. **HMC convergence.** The performance of an individual HMC sample and a BMA ensemble of 100 samples from each one of 3 HMC chains after the burn-in as a function of burn-in length. The dashed line indicates the burn-in length of 50 that we used in the main experiments in this paper. We use ResNet-20-FRN on CIFAR-10 and CNN-LSTM on IMDB. On IMDB, there is no visible dependence of the results on the burn-in length; on CIFAR-10, there is a weak trend that slows down over time.

study two-dimensional subspaces of the parameter space of the form

$$\mathcal{S} = \{w | w = w_1 \cdot a + w_2 \cdot b + w_3 \cdot (1 - a - b)\}. \quad (3)$$

$\mathcal{S}$ is the unique two-dimensional affine subspace (plane) of the parameter space that includes parameter vectors w_1, w_2 and w_3.

In Figure 3(a) we visualize the posterior log-density, log-likelihood and log-prior density of a ResNet-20-FRN on CIFAR-10. For the visualization, we use the subspace $\mathcal{S}$ defined by the parameter vectors w_1, w_{51} and w_{101}, the samples produced by HMC at iterations $1, 51$ and 101 after burn-in respectively. We observe that HMC is able to navigate complex geometry: the samples fall in three seemingly isolated modes in our two-dimensional cross-section of the posterior. In other words, HMC samples from a single chain are not restricted to any specific convex Gaussian-like mode, and instead explore a region of high posterior density of a complex shape in the parameter space. We note that popular approximate inference procedures, such as variational methods, and Laplace approximations, are typically constrained to unimodal Gaussian approximations to the posterior, which we indeed expect to miss a large space of compelling solutions in the posterior.

In Figure 3(b) we provide a visualization for the samples produced by 3 different HMC chains at iteration 51 after burn-in. Comparing the visualizations for samples from the same chain and samples from independent chains in Figure 3, we see that the shapes of the posterior surfaces are different, with the latter appearing more regular and symmetric. The qualitative differences between (a) and (b) suggest that while each HMC chain is able to navigate the posterior geometry the chains do not mix perfectly in the weight space, confirming our results in Section 5.1.

In Appendix D we provide additional details on our visualization procedure and visualizations using the CNN-LSTM on IMDB.

5.3. Convegence of the HMC chains

As another diagnostic, we look at the convergence of the performance of HMC BMA estimates and individual samples as a function of the length of the burn-in period. For a converged chain, the performance of the BMA and individual samples should be stationary not show any visible trends after a sufficiently long burn-in. We use the samples from 3 HMC chains, and evaluate performance of the ensemble of the first 100 HMC samples in each chain after discarding the first n_{bi} samples, where n_{bi} is the length of the burn-in. Additionally, we evaluate the performance of the individual HMC samples after n_{bi} iterations in each of the chains.

We report the results for ResNet-20-FRN on CIFAR-10 and CNN-LSTM on IMDB in Figure 4. On IMDB, there is no visible trend in performance, so a burn-in of just 10 HMC iterations should be sufficient. On CIFAR-10, we observe a slowly rising trend that saturates at about 50 iterations, indicating that a longer burn-in period is needed compared to IMDB. We therefore use a burn-in period of 50 HMC iterations on both CIFAR and IMDB for the remainder of the paper.

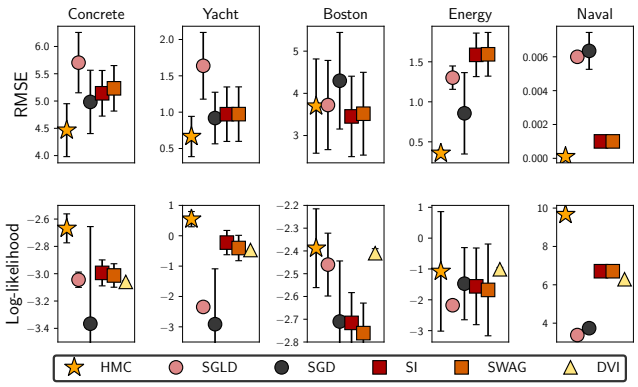

Figure 5. **UCI regression datasets.** Performance of Hamiltonian Monte Carlo (HMC), stochastic gradient Langevin dynamics (SGLD), stochastic gradient descent (SGD), subspace inference (SI) (Izmailov et al., 2019), SWAG (Maddox et al., 2019) and deterministic variational inference (DVI; Wu et al., 2018). We use a fully-connected architecture with a single hidden layer of 50 neurons. The results reported for each method are mean and standard deviation computed over 20 random train-test splits of the dataset. For SI, SWAG and DVI we report the results presented in Izmailov et al. (2019). **Top:** test root-mean-squared error. **Bottom:** test log-likelihood. HMC performs on par with or better than all other baselines in each experiment, often providing a significant improvement.

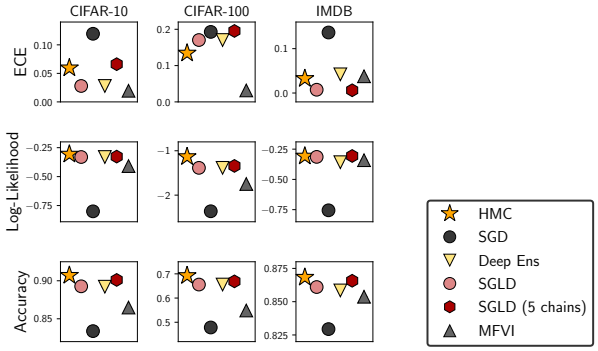

Figure 6. **Image and text classification.** Performance of Hamiltonian Monte Carlo (HMC), stochastic gradient Langevin dynamics (SGLD) with 1 and 5 chains, mean field variational inference (MFVI), stochastic gradient descent (SGD), and deep ensembles. We use ResNet-20-FRN on CIFAR datasets, and CNN-LSTM on IMDB. Bayesian neural networks via HMC outperform all baselines on all datasets in terms of accuracy and log-likelihood. On ECE, the methods perform comparably.

6. Evaluating Bayesian neural networks

Now that we have a procedure for effective HMC sampling, we are primed to explore exciting questions about the fundamental behaviour of Bayesian neural networks, such as the role of tempering, the prior over parameters, generalization performance, and robustness to covariate shift. In this section we evaluate Bayesian neural networks in various problems using our implementation of HMC. Throughout the experiments, we use posterior temperature $T = 1$.

We emphasize that the main goal of our paper and this section in particular is to *understand* the behaviour of true Bayesian neural network posteriors using HMC as a precise tool, and *not* to argue for HMC as a practical method for Bayesian deep learning.

Summary: Bayesian neural networks achieve strong results outperforming even large deep ensembles in a range of evaluations. Surprisingly, however, BNNs are *less* robust to distribution shift than conventionally-trained models.

6.1. Regression on UCI datasets

Bayesian deep learning methods are often evaluated on small-scale regression problems using fully connected networks (e.g., Wu et al., 2018; Izmailov et al., 2019; Maddox et al., 2019). Following these works, we evaluate Bayesian neural networks using HMC on five UCI regression datasets: *Concrete*, *Yacht*, *Boston*, *Energy* and *Naval*. For each of these datasets, we construct 20 random 90-to-10 train-test splits and report the mean and standard deviation of performance over the splits. We use a fully connected neural network with a single hidden layer of size 50 and 2 outputs representing the predictive mean and standard deviation. For HMC we used a single chain with 10 burn-in iterations and 90 iterations of sampling. For more details, please see Appendix A.

We report the results in Figure 5. HMC typically outperforms all the baselines, often by a significant margin, both in test RMSE and log-likelihood. On the *Boston* dataset, HMC achieves a slightly higher average RMSE compared to the subspace inference and SWAG (Izmailov et al., 2019; Maddox et al., 2019) but outperforms both these methods significantly in terms of log-likelihood.

6.2. Image Classification on CIFAR

Next, we evaluate Bayesian neural networks using HMC on image classification problems. We use the ResNet-20-FRN architecture on CIFAR-10 and CIFAR-100. We picked a random subset of 40960 of the 50000 images for each of the datasets to be able to evenly shard the data across the TPU devices; we use the same subset for both HMC and the baselines. We run 3 HMC chains using step size 10^{-5} and a prior variance of $1/5$, resulting in 70,248 leapfrog steps per sample. In each chain we discard the first 50 samples as burn-in, and then draw 240 samples (720 in total for

	AUC-ROC			
OOD DATASET	HMC	DE	ODIN	MAHAL.
CIFAR-100	0.857	0.853	0.858	**0.882**
SVHN	0.8814	0.8529	0.967	**0.991**

Table 1. **Out-of-distribution detection.** We use a ResNet-20-FRN model trained on CIFAR-10 to detect out-of-distribution data coming from SVHN or CIFAR-100. We report the results for HMC, deep ensembles and specialized ODIN (Liang et al., 2017) and Mahalanobis (Lee et al., 2018) methods. We report the AUC-ROC score (higher is better) evaluating the ability of each method to distinguish between in-distribution and OOD data. The predictive uncertainty from Bayesian neural networks allows us to detect OOD inputs: HMC outpefroms deep ensembles on both datasets. Furthermore, HMC is competitive with ODIN on the harder near-OOD task of detecting CIFAR-100 images, but underperforms on the easier far-OOD task of detecting SVHN images.

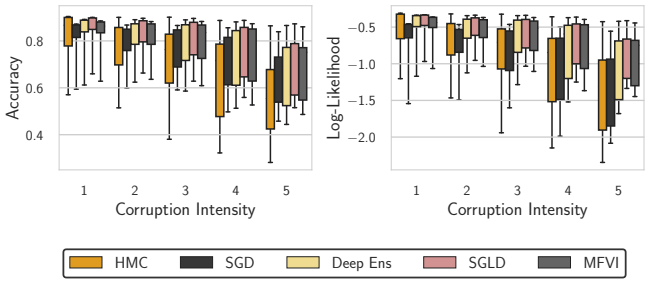

Figure 7. **Evaluation on CIFAR-10-C.** Accuracy and log-likelihood of HMC, SGD, deep ensembles, SGLD and MFVI on a distribution shift task, where the CIFAR-10 test set is corrupted in 16 different ways at various intensities on the scale of 1 to 5. We use the ResNet-20-FRN architecture. Boxes capture the quartiles of performance over each corruption, with the whiskers indicating the minimum and maximum. HMC is surprisingly the worst of the considered methods: even a single SGD solution provides better OOD robustness.

3 chains)[5]. For SGLD, we use a single chain with 1000 burn-in epochs and 9000 epochs of sampling producing 900 samples; we also report the performance of an ensemble of 5 independent SGLD chains. Next, we report the performance of a mean field variational inference (MFVI) solution; we initialize the mean of MFVI with a solution pre-trained with SGD and use an ensemble of 50 samples from the VI posterior at evaluation. Finally, we report the performance of a single SGD solution and a deep ensemble of 50 models. For more details, see Appendix A.

We report the results in Figure 6. Bayesian neural networks outperform all baselines in terms of accuracy and log-likelihood on both datasets. In terms of ECE, SGD provides the worst results across the board, and the rest of the methods are competitive; MFVI is particularly well-calibrated on CIFAR-100.

Out-of-distribution detection. Bayesian deep learning methods are often evaluated on out-of-distribution detection. In the Table 1 we report the performance of HMC-based Bayesian neural network on out-of-distribution (OOD) detection. To detect OOD data, we use the level of predicted confidence (value of the softmax class probability for the predicted class) from the HMC ensemble, measuring the area under the receiving operator characteristic curve (AUC-ROC). We train the methods on CIFAR-10 and use CIFAR-100 and SVHN as OOD data sources. We find that BNNs perform competitively with the specialized ODIN method in the challenging near-OOD detection setting (i.e. when the OOD data distribution is similar to the training data) of CIFAR-100, while underperforming in the easier far-OOD setting on SVHN relative to the baselines (Liang et al., 2017; Lee et al., 2018).

Robustness to distribution shift Bayesian methods are often specifically applied to covariate shift problems (Ovadia et al., 2019; Wilson & Izmailov, 2020; Dusenberry et al., 2020). We evaluate the the performance of HMC and Deep Ensemble-based Bayesian neural networks on the CIFAR-10-C dataset (Hendrycks & Dietterich, 2019), which applies a set of corruptions to CIFAR-10 with varying intensities. Mimicking the setup in Ovadia et al. (2019), we use the same 16 corruptions, evaluating the performance at all intensities. We report the results in Figure 7. Surprisingly, we find that Deep Ensembles and SGLD are consistently more robust to distribution shift than HMC-based BNNs. For high corruption intensities, even a single SGD model outperforms the HMC ensemble.

In Appendix F we provide further exploration of this effect, where we see HMC samples are significantly less robust to many types of noise compared to conventionally-trained SGD models. Interestingly, the performance of HMC-based BNNs under data corruption can be significantly improved by using posterior tempering.

6.3. Language Classification on IMDB

We use a CNN-LSTM architecture on the IMDB binary text classification dataset. In Figure 6 we report the results for HMC and the same baselines as in Section 6.2. We use HMC with a step size of 10^{-5} and a prior variance of $1/40$, resulting in 24,836 leapfrog steps per sample. We run 3 chains, burning-in for 50 samples, and drawing 400 samples per chain (1,200 total). For more details on the hyperparameters, please see Appendix A. Analogously to the image classification experiments, HMC outperforms

[5] In total, on CIFAR-10 our HMC run requires as many computations as *over 60 million epochs* of standard SGD training

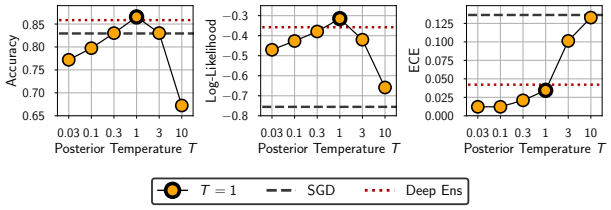

Figure 8. **Effect of posterior temperature.** The effect of posterior temperature T on the log-likelihood, accuracy and expected calibration error using the CNN-LSTM model on the IMDB dataset. For both the log-likelihood and accuracy $T = 1$ provides optimal performance, while for the ECE the colder posteriors provide a slight improvement. For all three metrics, the posterior at $T = 1$ outperforms the SGD baseline as well as a deep ensemble of 10 independently trained models.

the baselines on accuracy and log-likelihood and provides competitive performance on ECE.

7. Do we need cold posteriors?

Multiple works have considered tempering the posterior in Bayesian neural networks (e.g. Wenzel et al., 2020; Wilson & Izmailov, 2020; Zhang et al., 2020b; Ashukha et al., 2020; Aitchison, 2020). Specifically, we can consider a distribution

$$p_T(w|\mathcal{D}) \propto \big(p(\mathcal{D}|w) \cdot p(w)\big)^{1/T}, \tag{4}$$

where w are the parameters of the network, $\mathcal{D}$ is the training dataset, $p(\mathcal{D}|w)$ is the likelihood of $\mathcal{D}$ for the network with parameters w and T is the *temperature*. Note that at temperature $T = 1$, p_T corresponds to the standard Bayesian posterior over the parameters of the network. Temperatures $T < 1$ correspond to *cold posteriors*, distributions that are sharper than the Bayesian posterior. Similarly, temperatures $T > 1$ correspond to *warm posteriors* which are softer than the Bayesian posterior. See Appendix Figure 12(d) for a visualization of the log-likelihood density surface at different temperatures.

Wenzel et al. (2020) argue that Bayesian neural networks require a cold posterior, and the performance at temperature $T = 1$ is inferior to even a single model trained with SGD. The authors refer to this phenomenon as *the cold posteriors effect*. However, our results are different:

> **Summary**: We show that that cold posteriors are not needed to obtain near-optimal performance with Bayesian neural networks and may even hurt performance. We show that the cold posterior effect is largely an artifact of data augmentation.

7.1. Testing the cold posteriors effect

Wenzel et al. (2020) demonstrate the cold posteriors with two main experiments: ResNet-20 on CIFAR-10 and CNN-LSTM on IMDB. In these experiments the authors show poor performance at temperature $T = 1$, with strong benefits from decreasing the temperature. However, for the CIFAR-10 experiment, it is apparent (Wenzel et al., 2020, Appendix K, Figure 28) that the results at $T = 1$ are near-optimal for the ResNet on CIFAR-10 if data augmentation is turned off and batch normalization is replaced with filter response normalization, which is in fact necessary for a clear Bayesian interpretation of the inference procedure.

Furthermore, in Section 6, we show that Bayesian neural networks can achieve performance superior to SGD and even deep ensembles at temperature $T = 1$, in particular using the same ResNet-20-FRN model on CIFAR-10 and CNN-LSTM model on IMDB used by Wenzel et al. (2020).

To further understand the effect of posterior temperature T, we compare the performance of the CNN-LSTM model at different T using our Hamiltonian Monte Carlo sampler. In all runs we used a fixed prior variance $\alpha^2 = \frac{1}{40}$. We report the results in Figure 8. We find that the performance of the BNN at $T = 1$ is better than the SGD baseline as well as a deep ensemble of 50 independent models. Moreover, the performance at $T = 1$ is better compared to all other temperatures we tested in terms of both test accuracy and log-likelihood.

We also note that while posterior tempering does not seem necessary for good predictive performance with BNNs, it may be helpful under distribution shift. In Appendix F we show that decreasing the temperature can significantly improve the robustness of BNN predictions to noise in the test inputs. Wilson & Izmailov (2020) additionally argue that tempering may be a reasonable procedure in general, and is not necessarily at odds with Bayesian principles.

Role of data augmentation. Our results are in contrast with Wenzel et al. (2020), who argue that cold posteriors are needed for good performance with BNNs. In Appendix G we provide an additional study of what may have caused the poor performance of BNNs in Wenzel et al. (2020), using the code for inference provided by Wenzel et al. (2020). We identify data augmentation as the key factor responsible for the cold posterior effect, and also show that batch normalizing does not significantly influence this effect: when the data augmentation is turned off, we do not observe the cold posteriors effect. Data augmentation cannot be naively incorporated in the Bayesian neural network model (see the discussion in appendix K of Wenzel et al. (2020)), and arguably it may be reasonable to decrease the temperature when using data augmentation: intuitively, data augmentation increases the amount of data observed by the model,

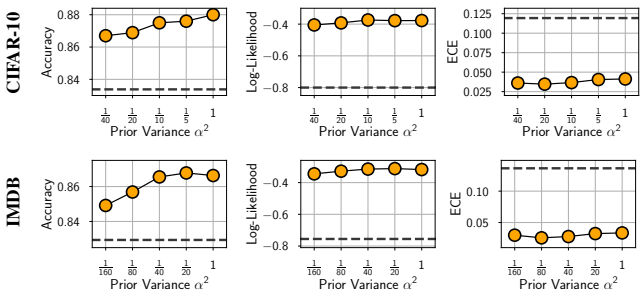

Figure 9. **Effect of prior variance.** The effect of prior variance on BNN performance. In each panel, the dashed line shows the performance of the SGD model from Section 6. While low prior variance may lead to over-regularization and hurt performance, all the considered prior scales lead to better results than the performance of an SGD-trained neural network of the same architecture.

and should lead to higher posterior contraction. We leave incorporating data augmentation in our HMC evaluation framework as an exciting direction of future work.

8. What is the effect of priors in Bayesian neural networks?

Bayesian deep learning is often criticized for the lack of intuitive priors over the parameters. For example, Wenzel et al. (2020) hypothesize that the popular Gaussian priors of the form $\mathcal{N}(0, \alpha^2 I)$ are inadequate and lead to poor performance. Tran et al. (2020) propose a new prior for Bayesian neural networks inspired by Gaussian processes (Rasmussen & Nickisch, 2010) based on this hypothesis. In concurrent work, Fortuin et al. (2021) also explore several alternatives to standard Gaussian priors inspired by the cold posteriors effect. Wilson & Izmailov (2020) on the other hand, argue that vague Gaussian priors in the parameter space induce useful function-space priors.

In Section 6 we have shown that Bayesian neural networks can achieve strong performance with vague Gaussian priors. In this section, we explore the sensitivity of BNNs to the choice of the prior scale as well as several alternative prior families, as a step towards a better understanding of the role of the prior in BNNs.

Summary: High-variance Gaussian priors over parameters of BNNs lead to strong performance. The results are robust with respect to the prior scale. Mixture of Gaussian and logistic priors over parameters are not too different in performance to Gaussian priors. These results highlight the relative importance of architecture over parameter priors in specifying a useful prior over functions.

PRIOR	GAUSSIAN	MOG	LOGISTIC
ACCURACY	0.866	0.863	**0.869**
ECE	0.029	0.025	**0.024**
LOG LIKELIHOOD	-0.311	-0.317	**-0.304**

Table 2. **Non-Gaussian priors.** BMA accuracy, ECE, and log-likelihood under different prior families using CNN-LSTM on IMDB. We produce 80 samples from a single HMC chain for each of the priors. The heavier-tailed logistic prior provides slightly better performance compared to the Gaussian and mixture of Gaussians (MoG) priors.

8.1. Effect of Gaussian prior scale

We use priors of the form $\mathcal{N}(0, \alpha^2 I)$ and vary the prior variance α^2. For all cases, we use a single HMC chain producing 40 samples. These are much shorter chains than the ones we used in Section 6, so the results are not as good; the purpose of this section is to explore the *relative* performance of BNNs under different priors.

We report the results for the CIFAR-10 and IMDB datasets in Figure 9. When the prior variance is too small, the regularization is too strong, hindering the performance. Setting the prior variance too large does not seem to hurt the performance as much. On both problems, the performance is fairly robust: a wide window of prior variances lead to strong performance. In particular, for all considered prior scales, the results are better than those of SGD training.

Why are BNNs so robust to the prior scale? One possible explanation for the relatively flat curves in Figure 9 is that large prior variances imply a strong prior belief that the "true" classifier (i.e., the model that would be learned given infinite data) should make high-confidence predictions. Since the model is powerful enough to achieve any desired training accuracy, the likelihood does not overrule this prior belief, and so the posterior assigns most of its mass to very confident classifiers. Past a certain point, increasing the prior variance on the weights may have no effect on the classifiers' already saturated probabilities. Consequently, nearly every member of the BMA may be highly overconfident. But the *ensemble* does not have to be overconfident—a mixture of overconfident experts can still make well-calibrated predictions. Appendix Figure 16 provides some qualitative evidence for this explanation; for some CIFAR-10 test set images, the HMC chain oscillates between assigning the true label probabilities near 1 and probabilities near 0.

8.2. Non-Gaussian priors

In Table 2, we report BMA accuracy, ECE, and log-likelihood for two non-Gaussian priors on the IMDB dataset: *logistic* and *mixture of Gaussians* (MoG). For the MoG prior we use a mixture of two Gaussians centered at 0, one with

Metric	HMC (reference)	SGD	Deep Ens	MFVI	SGMCMC			
					SGLD	SGHMC	SGHMC CLR	SGHMC CLR-Prec
CIFAR-10								
Accuracy	89.64 ±0.25	83.44 ±1.14	88.49 ±0.10	86.45 ±0.27	89.32 ±0.23	89.38 ±0.32	**89.63 ±0.37**	87.46 ±0.21
Agreement	94.01 ±0.25	85.48 ±1.00	91.52 ±0.06	88.75 ±0.24	91.54 ±0.15	91.98 ±0.35	**92.67 ±0.52**	90.96 ±0.24
Total Var	0.074 ±0.003	0.190 ±0.005	0.115 ±0.000	0.136 ±0.000	0.110 ±0.001	0.109 ±0.001	**0.099 ±0.006**	0.111 ±0.002
CIFAR-10-C								
Accuracy	70.91 ±0.93	71.04 ±1.80	76.99 ±0.39	75.40 ±0.34	**78.80 ±0.17**	78.20 ±0.25	76.43 ±0.39	73.42 ±0.39
Agreement	86.00 ±0.44	72.01 ±0.82	79.29 ±0.18	75.47 ±0.27	77.99 ±0.22	78.98 ±0.22	**80.93 ±0.73**	79.65 ±0.35
Total Var	0.133 ±0.004	0.334 ±0.007	0.220 ±0.003	0.245 ±0.002	0.214 ±0.002	0.203 ±0.002	**0.194 ±0.010**	0.205 ±0.005

Table 3. **Evaluation of cheaper alternatives to HMC.** Agreement and total variation between predictive distributions of HMC and approximate inference methods: deep ensembles, mean field variational inference (MFVI), and stochastic gradient Monte Carlo (SGMCMC) variations. For all methods we use ResNet-20-FRN trained on CIFAR-10 and evaluate predictions on the CIFAR-10 and CIFAR-10-C test sets. For CIFAR-10-C we report the average results across all corruptions and corruption intensities. We additionally report the results for HMC for reference: we compute the agreement and total variation between one of the chains and the ensemble of the other two chains. For each method we report the mean and standard deviation of the results over three independent runs. MFVI provides the worst approximation of the predictive distribution. Deep ensembles despite often being considered non-Bayesian, significantly outperform MFVI. SG-MCMC methods provide the best results with SGHMC-CLR showing the best overall performance.

variance $\frac{1}{40}$ and the other with variance $\frac{1}{160}$. We pick prior scale of the logistic prior to have a variance of $\frac{1}{40}$. We additionally provide the results for a Gaussian prior with variance $\frac{1}{40}$. We approximate the BMA using 80 samples from a single HMC chain for each of the priors. We find that the heavier-tailed logistic prior performs slightly better than the Gaussian and MoG.

8.3. Importance of Architecture in Prior Specification

We often think of the prior narrowly in terms of a distribution over parameters $p(w)$. But the prior that matters is the prior over functions $p(f(x))$ that is induced when a prior over parameters $p(w)$ is combined with the functional form of a neural network $f(x, w)$. All of the results in this section point to the relative importance of the architecture in defining the prior over functions, compared to the prior over parameters. A vague prior over parameters is not necessarily vague in function-space. Moreover, while the details of the prior distribution over parameters $p(w)$ have only a minor effect on performance, the choice of architecture certainly has a major effect on performance.

9. Do scalable BDL methods and HMC make similar predictions?

While HMC shows strong performance in our evaluation in Section 6, in most realistic BNN settings it is an impractical method. However, HMC can be used as a *reference* to evaluate and calibrate more scalable and practical alternatives. In this section, we evaluate the *fidelity* of SGMCMC, variational methods, and deep ensembles in representing the predictive distribution (Bayesian model average) given by our HMC reference.

Summary: While SGMCMC and Deep Ensembles can provide good generalization accuracy and calibration, their predictive distributions differ from HMC. Deep ensembles are similarly close to the HMC predictive distribution as SGLD, and closer than standard variational inference.

9.1. Comparing the predictive distributions

We consider two primary metrics: *agreement* and *total variation*. We define the agreement between the predictive distributions $\hat{p}$ of HMC and p of another method as the fraction of the test data points for which the top-1 predictions of $\hat{p}$ and p are the same:

$$\frac{1}{n}\sum_{i=1}^{n} I[\arg\max_j \hat{p}(y=j|x_i) = \arg\max_j p(y=j|x_i)],$$

where $I[\cdot]$ is the indicator function and n is the number of test data points x_i. We define the total variation metric between $\hat{p}$ and p as the total variation distance between the

predictive distributions averaged over the test data points:

$$\frac{1}{n}\sum_{i=1}^{n}\frac{1}{2}\sum_{j}\left|\hat{p}(y=j|x_i)-p(y=j|x_i)\right|.$$

The agreement (higher is better) captures how well a method is able to capture the top-1 predictions of HMC, while the total variation (lower is better) compares the predictive probabilities for each of the classes.

In Table 3 we report the agreement and total variation metrics as well as the predictive accuracy on the CIFAR-10 and CIFAR-10-C test sets for a deep ensemble of 50 models and several SGLD variations: standard SGLD (Welling & Teh, 2011), SGLD with momentum (SGHMC) (Chen et al., 2014), SGLD with momentum and a cyclical learning rate schedule (SGHMC-CLR) (Zhang et al., 2020b) and SGLD with momentum, cyclical learning rate schedule and a preconditioner (SGHMC-CLR-Prec) (Wenzel et al., 2020). All methods were trained on CIFAR-10. For more details, please see Appendix A.

Overall, the absolute value of agreement achieved by all methods is fairly low on CIFAR-10 and especially on CIFAR-10-C. More advanced SGHMC-CLR and SGHMC-CLR-Prec methods provide a better fit of the HMC predictive distribution while not necessarily improving the accuracy. Notably, these methods are also *less* robust to the data corruptions in CIFAR-10-C, again suggesting that higher fidelity representations of the predictive distribution can lead to decreased robustness to covariate shift, as we found in section 6.2.

Deep ensembles, while not typically considered to be a Bayesian method, provide a reasonable approximation to the HMC predictive distribution. In particular, deep ensembles outperform both SGLD and SGHMC in terms of total variation on CIFAR-10 and in terms of agreement on CIFAR-10-C. These results support the argument that deep ensembles, while not typically characterized as a Bayesian method, provide a *higher fidelity* approximation to a Bayesian model average than methods that are conventionally accepted as Bayesian inference procedures in modern deep learning (Wilson & Izmailov, 2020).

In Appendix F we explore the performance of HMC, SGD, deep ensembles, SGLD and SGHMC-CLR-Prec under different corruptions individually. Interestingly, the behavior of SGLD and SGHMC-CLR-Prec appears more similar to that of deep ensembles than that of HMC. So, while both SGMCMC and deep ensembles are very compelling practically, they provide relatively distinct predictive distributions from HMC. Mean-field variational inference methods are particularly far from the HMC predictive distribution. Thus, we should be very careful when making judgements about *true* Bayesian neural networks based on the SGMCMC or MFVI performance.

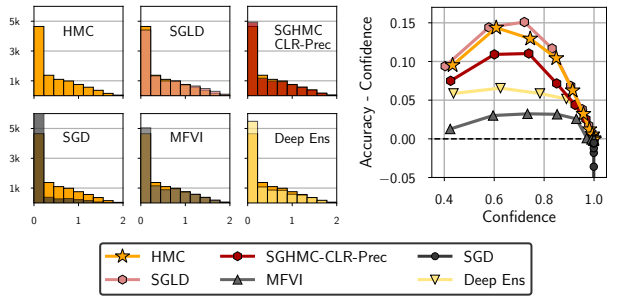

Figure 10. Distribution of predictive entropies (**left**) and calibration curve (**right**) of posterior predictive distributions for HMC, SGD, deep ensembles, MFVI, SGLD and SGHMC-CLR-Prec for ResNet20-FRN on CIFAR-10. On the left, for all methods, except HMC we plot a pair of histograms: for HMC and for the corresponding method. SGD, Deep ensembles and MFVI provide more confident predictions than HMC. SGMCMC methods appear to fit the predictive distribution of HMC better: SGLD is slightly underconfident relative to HMC while SGHMC-CLR-Prec is slightly over-confident.

9.2. Predictive entropy and calibration curves

To provide an additional comparison of the predictive distributions between HMC and other methods, in Figure 10 we visualize the distribution of predictive entropies and the calibration curves for HMC, SGD, deep ensembles, MFVI, SGLD and SGHMC-CLR-Prec on CIFAR-10 using ResNet-20-FRN.

All methods except fot SGD make conservative predictions: their confidences tend to underestimate their accuracies (Figure 10, right); SGD on the other hand is very over-confident (in agreement with the results in Guo et al., 2017). Deep ensembles and MFVI provide the most calibrated predictions, while SGLD and SGHMC-CLR-Prec match the HMC entropy distribution and calibration curve closer.

10. Discussion

Despite the rapidly increasing popularity of approximate Bayesian inference in modern deep learning, little is known about the behaviour of truly Bayesian neural networks. To the best of our knowledge, our work provides the first realistic evaluation of Bayesian neural networks with precise and exhaustive posterior sampling. We establish several properties of Bayesian neural networks, including good generalization performance, lack of a cold posterior effect, and a surprising lack of robustness to covariate shift. We hope that our observations and the tools that we develop will facilitate fundamental progress in understanding the behaviour of Bayesian neural networks.

Is HMC Converging? In general, it is not possible to ensure that an MCMC method has converged to sampling

from the true posterior distribution: theoretically, there may always remain regions of the posterior that cannot be discovered by the method but that contain most of the posterior mass. To maximize the performance of HMC, we choose the hyper-parameters that are the most likely to provide convergence: long trajectory lengths, and multiple long chains. In Section 5, we study the convergence of HMC using the available convergence diagnostics. We find that while HMC does not mix perfectly in weight space, in the space of predictions we cannot find evidence of non-mixing.

Should we use Bayesian neural networks? Our results show that Bayesian neural networks can improve the performance over models trained with SGD in a variety of settings, both in terms of uncertainty calibration and predictive accuracy. On most of the problems we considered in this work, the best results were achieved by Bayesian neural networks. We believe that our results provide motivation to use Bayesian neural networks with accurate posterior approximation in practical applications.

Should we use HMC in practice? For most realistic scenarios in Bayesian Deep Learning, HMC is an impractical method. On the image classification benchmarks, HMC takes orders of magnitude more compute than any of the baselines that we considered. We hope that our work will inspire the community to produce new accurate and scalable approximate inference methods for Bayesian deep learning.

10.1. Challenging conventional wisdom

A conventional wisdom has emerged that deep ensembles are a non-Bayesian alternative to variational methods, that standard priors for neural networks are poor, and that cold posteriors are a problematic result for Bayesian deep learning. Our results highlight that one should take care in uncritically repeating such claims. In fact, deep ensembles appear to provide a higher fidelity representation of the Bayesian predictive distribution than widely accepted approaches to approximate Bayesian inference. If anything, the takeaway from the relatively good performance of deep ensembles is that we would benefit from approximate inference being *closer* to the Bayesian ideal! Moreover, the details over the priors in weight space can have a relatively minor effect on performance, and there is no strong evidence that standard Gaussian priors are particularly bad. In fact, there are many reasons to believe these priors have useful properties (Wilson & Izmailov, 2020). Similarly, on close inspection, we found no evidence for a general cold posterior effect, which we identify as largely an artifact of data augmentation. Although we see here that tempering does not in fact seem to be required, as argued in Wilson & Izmailov (2020) tempering is also not necessarily unreasonable or even divergent from Bayesian principles.

Even the results we found that are less favourable to Bayesian deep learning are contrary to the current orthodoxy. Indeed, higher fidelity Bayesian inference surprisingly appears to suffer more greatly from covariate shift, despite the popularity of approximate Bayesian inference procedures in this setting.

Acknowledgements

The authors would like to thank many people at Google for many helpful discussions and much helpful feedback, especially Rodolphe Jenatton, Rif A. Saurous, Jasper Snoek, Pavel Sountsov, Florian Wenzel, and the entire TensorFlow Probability team. This research is supported by an Amazon Research Award, NSF I-DISRE 193471, NIH R01DA048764-01A1, NSF IIS-1910266, and NSF 1922658NRT-HDR: FUTURE Foundations, Translation, and Responsibility for Data Science.

References

Ahn, S., Korattikara, A., and Welling, M. Bayesian posterior sampling via stochastic gradient fisher scoring. *arXiv preprint arXiv:1206.6380*, 2012.

Ahn, S., Shahbaba, B., and Welling, M. Distributed stochastic gradient mcmc. In *International conference on machine learning*, pp. 1044–1052. PMLR, 2014.

Aitchison, L. A statistical theory of cold posteriors in deep neural networks. *arXiv preprint arXiv:2008.05912*, 2020.

Ashukha, A., Lyzhov, A., Molchanov, D., and Vetrov, D. Pitfalls of in-domain uncertainty estimation and ensembling in deep learning. *arXiv preprint arXiv:2002.06470*, 2020.

Betancourt, M. The fundamental incompatibility of hamiltonian monte carlo and data subsampling. *arXiv preprint arXiv:1502.01510*, 2015.

Blundell, C., Cornebise, J., Kavukcuoglu, K., and Wierstra, D. Weight uncertainty in neural networks. *arXiv preprint arXiv:1505.05424*, 2015.

Bradbury, J., Frostig, R., Hawkins, P., Johnson, M. J., Leary, C., Maclaurin, D., Necula, G., Paszke, A., VanderPlas, J., Wanderman-Milne, S., and Zhang, Q. JAX: composable transformations of Python+NumPy programs, 2018. URL http://github.com/google/jax.

Chen, T., Fox, E., and Guestrin, C. Stochastic gradient hamiltonian monte carlo. In *International conference on machine learning*, pp. 1683–1691. PMLR, 2014.

Cobb, A. D. and Jalaian, B. Scaling hamiltonian monte carlo inference for bayesian neural networks with symmetric splitting. *arXiv preprint arXiv:2010.06772*, 2020.

Cranmer, M., Tamayo, D., Rein, H., Battaglia, P., Hadden, S., Armitage, P., Ho, S., and Spergel, D. N. A bayesian neural network predicts the dissolution of compact planetary systems. 2021.

Daxberger, E., Nalisnick, E., Allingham, J. U., Antorán, J., and Hernández-Lobato, J. M. Expressive yet tractable bayesian deep learning via subnetwork inference. *arXiv preprint arXiv:2010.14689*, 2020.

Ding, N., Fang, Y., Babbush, R., Chen, C., Skeel, R., and Neven, H. Bayesian sampling using stochastic gradient thermostats. 2014.

Draxler, F., Veschgini, K., Salmhofer, M., and Hamprecht, F. A. Essentially no barriers in neural network energy landscape. *arXiv preprint arXiv:1803.00885*, 2018.

Dusenberry, M., Jerfel, G., Wen, Y., Ma, Y., Snoek, J., Heller, K., Lakshminarayanan, B., and Tran, D. Efficient and scalable bayesian neural nets with rank-1 factors. In *International conference on machine learning*, pp. 2782–2792. PMLR, 2020.

Elfwing, S., Uchibe, E., and Doya, K. Sigmoid-weighted linear units for neural network function approximation in reinforcement learning. *Neural Networks*, 107:3–11, 2018.

Farquhar, S., Smith, L., and Gal, Y. Liberty or depth: Deep bayesian neural nets do not need complex weight posterior approximations. *arXiv preprint arXiv:2002.03704*, 2020.

Filos, A., Farquhar, S., Gomez, A. N., Rudner, T. G., Kenton, Z., Smith, L., Alizadeh, M., de Kroon, A., and Gal, Y. A systematic comparison of bayesian deep learning robustness in diabetic retinopathy tasks. *arXiv preprint arXiv:1912.10481*, 2019.

Foong, A. Y., Burt, D. R., Li, Y., and Turner, R. E. On the expressiveness of approximate inference in bayesian neural networks. *arXiv preprint arXiv:1909.00719*, 2019.

Fort, S., Hu, H., and Lakshminarayanan, B. Deep ensembles: A loss landscape perspective. *arXiv preprint arXiv:1912.02757*, 2019.

Fortuin, V., Garriga-Alonso, A., Wenzel, F., Rätsch, G., Turner, R., van der Wilk, M., and Aitchison, L. Bayesian neural network priors revisited. *arXiv preprint arXiv:2102.06571*, 2021.

Gal, Y. *Uncertainty in deep learning*. PhD thesis, PhD thesis, University of Cambridge, 2016.

Gal, Y. and Ghahramani, Z. Dropout as a Bayesian approximation: Representing model uncertainty in deep learning. In *international conference on machine learning*, pp. 1050–1059, 2016.

Gal, Y., Hron, J., and Kendall, A. Concrete dropout. *arXiv preprint arXiv:1705.07832*, 2017.

Garipov, T., Izmailov, P., Podoprikhin, D., Vetrov, D. P., and Wilson, A. G. Loss surfaces, mode connectivity, and fast ensembling of DNNs. In *Neural Information Processing Systems*, 2018.

Garriga-Alonso, A. and Fortuin, V. Exact langevin dynamics with stochastic gradients. *arXiv preprint arXiv:2102.01691*, 2021.

Gelman, A., Rubin, D. B., et al. Inference from iterative simulation using multiple sequences. *Statistical science*, 7(4):457–472, 1992.

Geneva, N. and Zabaras, N. Modeling the dynamics of pde systems with physics-constrained deep auto-regressive networks. *Journal of Computational Physics*, 403: 109056, 2020.

Graves, A. Practical variational inference for neural networks. In *Advances in neural information processing systems*, pp. 2348–2356. Citeseer, 2011.

Guo, C., Pleiss, G., Sun, Y., and Weinberger, K. Q. On calibration of modern neural networks. In *Proceedings of the 34th International Conference on Machine Learning-Volume 70*, pp. 1321–1330. JMLR. org, 2017.

He, K., Zhang, X., Ren, S., and Sun, J. Deep residual learning for image recognition. In *Proceedings of the IEEE conference on computer vision and pattern recognition*, pp. 770–778, 2016.

Hendrycks, D. and Dietterich, T. Benchmarking neural network robustness to common corruptions and perturbations. *arXiv preprint arXiv:1903.12261*, 2019.

Hendrycks, D. and Gimpel, K. Gaussian error linear units (gelus). *arXiv preprint arXiv:1606.08415*, 2016.

Hernández-Lobato, J. M. and Adams, R. Probabilistic backpropagation for scalable learning of bayesian neural networks. In *International Conference on Machine Learning*, pp. 1861–1869. PMLR, 2015.

Hochreiter, S. and Schmidhuber, J. Long short-term memory. *Neural computation*, 9(8):1735–1780, 1997.

Hoffman, M. D., Blei, D. M., Wang, C., and Paisley, J. Stochastic variational inference. *The Journal of Machine Learning Research*, 14(1):1303–1347, 2013.

Ioffe, S. and Szegedy, C. Batch normalization: Accelerating deep network training by reducing internal covariate shift. *arXiv preprint arXiv:1502.03167*, 2015.

Izmailov, P., Podoprikhin, D., Garipov, T., Vetrov, D., and Wilson, A. G. Averaging weights leads to wider optima and better generalization. In *Uncertainty in Artificial Intelligence (UAI)*, 2018.

Izmailov, P., Maddox, W. J., Kirichenko, P., Garipov, T., Vetrov, D., and Wilson, A. G. Subspace inference for Bayesian deep learning. *Uncertainty in Artificial Intelligence*, 2019.

Jouppi, N. P., Yoon, D. H., Kurian, G., Li, S., Patil, N., Laudon, J., Young, C., and Patterson, D. A domain-specific supercomputer for training deep neural networks. *Communications of the ACM*, 63(7):67–78, 2020.

Kendall, A. and Gal, Y. What uncertainties do we need in Bayesian deep learning for computer vision? In *Advances in neural information processing systems*, pp. 5574–5584, 2017.

Khan, M. E., Nielsen, D., Tangkaratt, V., Lin, W., Gal, Y., and Srivastava, A. Fast and scalable Bayesian deep learning by weight-perturbation in adam. *arXiv preprint arXiv:1806.04854*, 2018.

Kingma, D. P., Salimans, T., and Welling, M. Variational dropout and the local reparameterization trick. *arXiv preprint arXiv:1506.02557*, 2015.

Kirkpatrick, J., Pascanu, R., Rabinowitz, N., Veness, J., Desjardins, G., Rusu, A. A., Milan, K., Quan, J., Ramalho, T., Grabska-Barwinska, A., et al. Overcoming catastrophic forgetting in neural networks. *Proceedings of the national academy of sciences*, 114(13):3521–3526, 2017.

Krizhevsky, A., Nair, V., and Hinton, G. The CIFAR-10 dataset. 2014. http://www.cs.toronto.edu/kriz/cifar.html.

Lakshminarayanan, B., Pritzel, A., and Blundell, C. Simple and scalable predictive uncertainty estimation using deep ensembles. In *Advances in Neural Information Processing Systems*, pp. 6402–6413, 2017.

Lao, J., Suter, C., Langmore, I., Chimisov, C., Saxena, A., Sountsov, P., Moore, D., Saurous, R. A., Hoffman, M. D., and Dillon, J. V. tfp. mcmc: Modern markov chain monte carlo tools built for modern hardware. *arXiv preprint arXiv:2002.01184*, 2020.

Lee, K., Lee, K., Lee, H., and Shin, J. A simple unified framework for detecting out-of-distribution samples and adversarial attacks. In *Advances in Neural Information Processing Systems*, pp. 7167–7177, 2018.

Li, D. X. On default correlation: A copula function approach. *Journal of Fixed Income*, 9(4):43–54, 2000.

Liang, S., Li, Y., and Srikant, R. Enhancing the reliability of out-of-distribution image detection in neural networks. *arXiv preprint arXiv:1706.02690*, 2017.

Liu, X., Xue, W., Xiao, L., and Zhang, B. Pbodl: Parallel bayesian online deep learning for click-through rate prediction in tencent advertising system. *arXiv preprint arXiv:1707.00802*, 2017.

Louizos, C. and Welling, M. Multiplicative normalizing flows for variational bayesian neural networks. In *International Conference on Machine Learning*, pp. 2218–2227. PMLR, 2017.

Ma, Y.-A., Chen, T., and Fox, E. B. A complete recipe for stochastic gradient mcmc. *arXiv preprint arXiv:1506.04696*, 2015.

Maas, A. L., Daly, R. E., Pham, P. T., Huang, D., Ng, A. Y., and Potts, C. Learning word vectors for sentiment analysis. In *Proceedings of the 49th Annual Meeting of the Association for Computational Linguistics: Human Language Technologies*, pp. 142–150, Portland, Oregon, USA, June 2011. Association for Computational Linguistics. URL http://www.aclweb.org/anthology/P11-1015.

MacKay, D. J. A practical bayesian framework for backpropagation networks. *Neural computation*, 4(3):448–472, 1992.

MacKay, D. J. Probable networks and plausible predictions?a review of practical Bayesian methods for supervised neural networks. *Network: computation in neural systems*, 6(3):469–505, 1995.

Maddox, W. J., Izmailov, P., Garipov, T., Vetrov, D. P., and Wilson, A. G. A simple baseline for Bayesian uncertainty in deep learning. In *Advances in Neural Information Processing Systems*, 2019.

Mandt, S., Hoffman, M. D., and Blei, D. M. Stochastic gradient descent as approximate Bayesian inference. *The Journal of Machine Learning Research*, 18(1):4873–4907, 2017.

Molchanov, D., Ashukha, A., and Vetrov, D. Variational dropout sparsifies deep neural networks. In *International Conference on Machine Learning*, pp. 2498–2507. PMLR, 2017.

Neal, R. *Bayesian Learning for Neural Networks*. Springer Verlag, 1996. ISBN 0387947248.

Neal, R. M. et al. Mcmc using hamiltonian dynamics. *Handbook of markov chain monte carlo*, 2(11):2, 2011.

Osawa, K., Swaroop, S., Jain, A., Eschenhagen, R., Turner, R. E., Yokota, R., and Khan, M. E. Practical deep learning with bayesian principles. *arXiv preprint arXiv:1906.02506*, 2019.

Ovadia, Y., Fertig, E., Ren, J., Nado, Z., Sculley, D., Nowozin, S., Dillon, J. V., Lakshminarayanan, B., and Snoek, J. Can you trust your model's uncertainty? evaluating predictive uncertainty under dataset shift. *arXiv preprint arXiv:1906.02530*, 2019.

Ramachandran, P., Zoph, B., and Le, Q. V. Searching for activation functions. *arXiv preprint arXiv:1710.05941*, 2017.

Rasmussen, C. E. and Nickisch, H. Gaussian processes for machine learning (GPML) toolbox. *Journal of Machine Learning Research (JMLR)*, 11:3011–3015, Nov 2010.

Ritter, H., Botev, A., and Barber, D. A scalable Laplace approximation for neural networks. In *International Conference on Learning Representations (ICLR)*, 2018.

Singh, S. and Krishnan, S. Filter response normalization layer: Eliminating batch dependence in the training of deep neural networks. In *Proceedings of the IEEE/CVF Conference on Computer Vision and Pattern Recognition*, pp. 11237–11246, 2020.

Srivastava, N., Hinton, G., Krizhevsky, A., Sutskever, I., and Salakhutdinov, R. Dropout: a simple way to prevent neural networks from overfitting. *The journal of machine learning research*, 15(1):1929–1958, 2014.

Tran, B.-H., Rossi, S., Milios, D., and Filippone, M. All you need is a good functional prior for bayesian deep learning. *arXiv preprint arXiv:2011.12829*, 2020.

Welling, M. and Teh, Y. W. Bayesian learning via stochastic gradient langevin dynamics. In *Proceedings of the 28th international conference on machine learning (ICML-11)*, pp. 681–688, 2011.

Wenzel, F., Roth, K., Veeling, B. S., Świątkowski, J., Tran, L., Mandt, S., Snoek, J., Salimans, T., Jenatton, R., and Nowozin, S. How good is the Bayes posterior in deep neural networks really? *arXiv preprint arXiv:2002.02405*, 2020.

Wilson, A. G. and Izmailov, P. Bayesian deep learning and a probabilistic perspective of generalization. *arXiv preprint arXiv:2002.08791*, 2020.

Wu, A., Nowozin, S., Meeds, E., Turner, R. E., Hernández-Lobato, J. M., and Gaunt, A. L. Deterministic variational inference for robust Bayesian neural networks. *arXiv preprint arXiv:1810.03958*, 2018.

Yao, J., Pan, W., Ghosh, S., and Doshi-Velez, F. Quality of uncertainty quantification for bayesian neural network inference. *arXiv preprint arXiv:1906.09686*, 2019.

Zhang, G., Sun, S., Duvenaud, D., and Grosse, R. Noisy natural gradient as variational inference. In *International Conference on Machine Learning*, pp. 5852–5861. PMLR, 2018.

Zhang, R., Cooper, A. F., and De Sa, C. Amagold: Amortized metropolis adjustment for efficient stochastic gradient mcmc. In *International Conference on Artificial Intelligence and Statistics*, pp. 2142–2152. PMLR, 2020a.

Zhang, R., Li, C., Zhang, J., Chen, C., and Wilson, A. G. Cyclical stochastic gradient MCMC for Bayesian deep learning. In *International Conference on Learning Representations*, 2020b.

Method	Hyper-parameter	Was Tuned	Experiments: CIFAR-10 ResNet-20-FRN	Experiments: CIFAR-100 ResNet-20-FRN	Experiments: IMDB CNN LSTM
HMC	Prior Variance	✓	$\frac{1}{5}$	$\frac{1}{5}$	$\frac{1}{40}$
	Step Size	✓	10^{-5}	10^{-5}	10^{-5}
	Num. Burnin Iterations	✗	50	50	50
	Num. Samples per Chain	✗	240	40	400
	Num. of Chains	✗	3	3	3
	Total Samples	✗	720	120	1200
	Total Epochs		$5 \cdot 10^7$	$8.5 \cdot 10^6$	$3 \cdot 10^7$
SGD	Weight Decay	✓	10	10	3
	Initial Step Size	✓	$3 \cdot 10^{-7}$	$1 \cdot 10^{-6}$	$3 \cdot 10^{-7}$
	Step Size Schedule	✗	cosine	cosine	cosine
	Batch Size	✓	80	80	80
	Num. Epochs	✗	500	500	500
	Momentum	✗	0.9	0.9	0.9
	Total Epochs		$5 \cdot 10^2$	$5 \cdot 10^2$	$5 \cdot 10^2$
Deep Ensembles	Num. Models	✗	50	50	50
	Total Epochs		$2.5 \cdot 10^4$	$2.5 \cdot 10^4$	$2.5 \cdot 10^4$
SGLD	Prior Variance	✓	$\frac{1}{5}$	$\frac{1}{5}$	$\frac{1}{5}$
	Step Size	✓	10^{-6}	$3 \cdot 10^{-6}$	$1 \cdot 10^{-5}$
	Step Size Schedule	✓	constant	constant	constant
	Batch Size	✓	80	80	80
	Num. Epochs	✗	10000	10000	10000
	Num. Burnin Epochs	✗	1000	1000	1000
	Num. Samples per Chain	✗	900	900	900
	Num. of Chains	✗	5	5	5
	Total Samples	✗	4500	4500	4500
	Total Epochs		$5 \cdot 10^4$	$5 \cdot 10^4$	$5 \cdot 10^4$
MFVI	Prior Variance	✗	$\frac{1}{5}$	$\frac{1}{5}$	$\frac{1}{5}$
	Num. Epochs	✗	300	300	300
	Optimizer	✓	Adam	Adam	Adam
	Initial Step Size	✓	10^{-4}	10^{-4}	10^{-4}
	Step Size Schedule	✗	cosine	cosine	cosine
	Batch Size	✓	80	80	80
	VI mean init	✗	SGD solution	SGD solution	SGD solution
	VI variance init	✓	10^{-2}	10^{-2}	10^{-2}
	Number of samples	✗	50	50	50
	Total Epochs		$8 \cdot 10^2$	$8 \cdot 10^2$	$8 \cdot 10^2$

Table 4. **Hyper-parameters for CIFAR and IMDB.** We report the hyper-parameters for each method our main evaluations on CIFAR and IMDB datasets in Section 6. For each method we report the total number of training epochs equivalent to the amount of compute spent. We run HMC on a cluster of 512 TPUs, and the baselines on a cluster of 8 TPUs. For each of the hyper-parameters we report whether it was tuned via cross-validation, or whether a value was selected without tuning.

Method	Hyper-parameter	Was Tuned	Experiments				
			Concrete	Yacht	Energy	Boston	Naval
HMC	Prior Variance	✓	$\frac{1}{10}$	$\frac{1}{10}$	$\frac{1}{10}$	$\frac{1}{10}$	$\frac{1}{40}$
	Step Size	✓	10^{-5}	10^{-5}	10^{-5}	10^{-5}	$5 \cdot 10^{-7}$
	Num. Burnin Iterations	✗	10	10	10	10	10
	Num. Iterations	✗	90	90	90	90	90
	Num. of Chains	✗	1	1	1	1	1
SGD	Weight Decay	✓	10	10^{-1}	10	10^{-1}	1
	Initial Step Size	✓	$3 \cdot 10^{-5}$	$3 \cdot 10^{-6}$	$3 \cdot 10^{-6}$	$3 \cdot 10^{-6}$	10^{-6}
	Step Size Schedule	✗	cosine	cosine	cosine	cosine	cosine
	Batch Size	✗	927	277	691	455	10740
	Num. Epochs	✓	1000	5000	5000	500	1000
	Momentum	✗	0.9	0.9	0.9	0.9	0.9
SGLD	Prior Variance	✓	$\frac{1}{10}$	$\frac{1}{10}$	$\frac{1}{10}$	$\frac{1}{10}$	1
	Step Size	✓	$3 \cdot 10^{-5}$	10^{-4}	$3 \cdot 10^{-5}$	$3 \cdot 10^{-5}$	10^{-6}
	Step Size Schedule	✗	constant	constant	constant	constant	constant
	Batch Size	✗	927	277	691	455	10740
	Num. Epochs	✗	10000	10000	10000	10000	10000
	Num. Burnin Epochs	✗	1000	1000	1000	1000	1000
	Num. Samples per Chain	✗	900	900	900	900	900
	Num. of Chains	✗	1	1	1	1	1

Table 5. **Hyper-parameters for UCI.** We report the hyper-parameters for each method our main evaluations on UCI datasets in Section 6. For HMC, the number of iterations is the number of HMC iterations after the burn-in phase; the number of accepted samples is lower. For each of the hyper-parameters we report whether it was tuned via cross-validation, or whether a value was selected without tuning.

Hyper-parameter	Was Tuned	SGLD	SGHMC	SGHMC CLR	SGHMC CLR-Prec
Initial Step Size	✓	10^{-6}	$3 \cdot 10^{-7}$	$3 \cdot 10^{-7}$	$3 \cdot 10^{-5}$
Step Size Schedule	✗	constant	constant	cyclical	cyclical
Momentum	✓	0.	0.9	0.95	0.95
Preconditioner	✗	None	None	None	RMSprop
Num. Samples per Chain	✗	900	900	180	180
Num. of Chains	✗	3	3	3	3

Table 6. **SGMCMC hyper-parameters on CIFAR-10.** We report the hyper-parameter values used by each of the SGMCMC methods in Section 9. The remaining hyper-parameters are the same as the SGLD hyper-parameters reported in Table 4. For each of the hyper-parameters we report whether it was tuned via cross-validation, or whether a value was selected without tuning.

Appendix Outline

This appendix is organized as follows. We present the Hamiltonian Monte Carlo algorithm that we implement in the paper in Algorithm 1, Algorithm 2. In Appendix A we provide the details on hyper-parameters used in our experiments. In Appendix B we provide a description of the $\hat{R}$ statistic used in Section 5.1. In Appendix C we study the marginals of the posterior over parameters estimated by HMC. In Appendix D we provide additional posterior density surface visualizations. In Appendix E we compare the BMA predictions using two independent HMC chains on a synthetic regression problem. In Appendix F we show that BNNs are not robust to distribution shift and discuss the reasons for this behavior. In Appendix G we provide a further discussion of the effect of posterior temperature. Finally, in Appendix H we visualize the predictions of HMC samples from a single chain on several CIFAR-10 test inputs.

A. Hyper-Parameters and Details

CIFAR and IMDB. In Table 4 we report the hyperparameters used by each of the methods in our main evaluation on CIFAR and IMDB datasets in Section 6. HMC was run on a cluster of 512 TPUs and the other baselines were run on a cluster of 8 TPUs. On CIFAR datasets the methods used a subset of 40960 datapoints. All methods were ran at posterior temperature 1. We tuned the hyper-parameters for all methods via cross-validation maximizing the accuracy on a validation set. For the step-sizes we considered an exponential grid with a step of $\sqrt{10}$ with 5-7 different values, where the boundaries were selected for each method so it would not

diverge. We considered weight decays $1, 5, 10, 20, 40, 100$ and the corresponding prior variances. For batch sizes we considered values 80, 200, 400 and 1000; for all methods lower batch sizes resulted in the best performance. For HMC we set the trajectory length according to the strategy described in Section 4.1. For SGLD, we experimented with using a cosine learning rate schedule decaying to a non-zero final step size, but it did not improve upon a constant schedule. For MFVI we experimented with the SGD and Adam optimizers; we initialize the mean of the MFVI distribution with a pre-trained SGD solution, and the per-parameter variance with a value $\sigma^{\text{VI}}_{\text{Init}}$; we tested values $10^{-2}, 10^{-1}, 10^{0}$ for $\sigma^{\text{VI}}_{\text{Init}}$. For all HMC hyper-parameters, we provide ablations illustrating their effect in Section 4. Producing a single sample with HMC on CIFAR datasets takes roughly one hour on our hardware, and on IMDB it takes 105 seconds; we can run up to three chains in parallel.

Temperature scaling on IMDB. For the experiments in Section 7 we run a single HMC chain producing 40 samples after 10 burn-in epochs for each temperature. We used step-sizes $5 \cdot 10^{-5}$, $3 \cdot 10^{-5}$, 10^{-5}, $3 \cdot 10^{-6}$, 10^{-6} and $3 \cdot 10^{-7}$ for temperatures 10, 3, 1, 0.3, 0.1 and 0.03 respectively, ensuring that the accept rates were close to 100%. We used a prior variance of $1/50$ in all experiments; the lower prior variance compared to Table 4 was chosen to reduce the number of leapfrog iterations, as we chose the trajectory length according to the strategy described in Section 4.1. We ran the experiments on 8 NVIDIA Tesla V-100 GPUs, as we found that sampling at low temperatures requires `float64` precision which is not supported on TPUs.

UCI Datasets. In Table 5 we report the hyperparameters used by each of the methods in our main evaluation on UCI datasets in Section 6. For each datasets we construct 20 random splits with 90% of the data in the train and 10% of the data in the test split. In the evaluation, we report the mean and standard deviation of the results across the splits. We use another random split for cross-validation to tune the hyper-parameters. For all datasets we use a fully-connected network with a single hidden layer with 50 neurons and 2 outputs representing the predictive mean and variance for the given input. We use a Gaussian likelihood to train each of the methods. For the SGD and SGLD baselines, we did not use mini-batches: the gradients were computed over the entire dataset. We run each experiment on a single NVIDIA Tesla V-100 GPU.

SGMCMC Methods. In Table 6 we report the hyper-parameters of the SGMCMC methods on the CIFAR-10 dataset used in the evaluation in Section 9. We considered momenta in the set of $\{0.9, 0.95, 0.99\}$ and step sizes in $\{10^{-4}, 3 \cdot 10^{-5}, 10^{-5}, 3 \cdot 10^{-6}, 10^{-6}, 3 \cdot 10^{-7}, 10^{-7}\}$. We selected the hyper-parameters with the best accuracy on the validation set. SGLD does not allow a momentum.

Algorithm 1 Hamiltonian Monte Carlo

Input: Trajectory length τ, number of burn-in interations N_{burnin}, initial parameters w_{init}, step size Δ, number of samples K, unnormalized posterior log-density function $f(w) = \log p(D|w) + \log p(w)$.
Output: Set S of samples w of the parameters.

$w \leftarrow w_{\text{init}}$; $\quad N_{\text{leapfrog}} \leftarrow \frac{\tau}{\Delta}$;
# Burn-in stage
for $i \leftarrow 1 \dots N_{\text{burnin}}$ **do**
  $m \sim \mathcal{N}(0, I)$;
  $(w, m) \leftarrow \text{Leapfrog}(w, m, \Delta, N_{\text{leapfrog}}, f)$;
end for
# Sampling
$S \leftarrow \varnothing$;
for $i \leftarrow 1 \dots K$ **do**
  $m \sim \mathcal{N}(0, I)$;
  $(w', m') \leftarrow \text{Leapfrog}(w, m, \Delta, N_{\text{leapfrog}}, f)$;
  # Metropolis-Hastings correction
  $p_{\text{accept}} \leftarrow \min\left\{1, \frac{f(w')}{f(w)} \cdot \exp\left(\frac{1}{2}\|m\|^2 - \|m'\|^2\right)\right\}$;
  $u \sim \text{Uniform}[0, 1]$;
  if $u \leq p_{\text{accept}}$ **then**
    $w \leftarrow w'$;
  end if
  $S \leftarrow S \cup \{w\}$;
end for

Algorithm 2 Leapfrog integration

Input: Parameters w_0, initital momentum m_0, step size Δ, number of leapfrog steps N_{leapfrog}, posterior log-density function $f(w) = \log p(w|D)$.
Output: New parameters w; new momentum m.

$w \leftarrow w_0$; $\quad m \leftarrow m_0$;
for $i \leftarrow 1 \dots N_{\text{leapfrog}}$ **do**
  $m \leftarrow m + \frac{\Delta}{2} \cdot \nabla f(w)$;
  $w \leftarrow w + \Delta \cdot m$;
  $m \leftarrow m + \frac{\Delta}{2} \cdot \nabla f(w)$;
end for
$\text{Leapfrog}(w_0, m_0, \Delta, N_{\text{leapfrog}}, f) \leftarrow (w, m)$

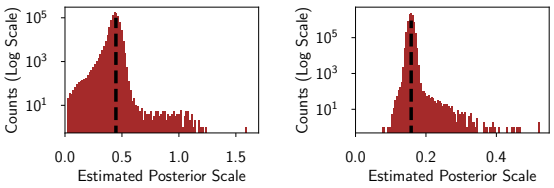

(a) ResNet-20-FRN (b) CNN-LSTM

Figure 11. **Marginal distributions of the weights.** Log-scale histograms of estimated marginal posterior standard deviations for ResNet-20-FRN on CIFAR-10 and CNN-LSTM on IMDB. The histograms show how many parameters have empirical standard deviations that fall within a given bin. For most of the parameters (notice that the plot is logarithmic) the posterior scale is very similar to that of the prior distribution.

B. Description of $\hat{R}$ Statistics

$\hat{R}$ (Gelman et al., 1992) is a popular MCMC convergence diagnostic. It is defined in terms of some scalar function $\psi(\theta)$ of the Markov chain iterates $\{\theta_{mn} | m \in \{1, \ldots, M\}, n \in \{1, \ldots, N\}\}$, where θ_{mn} denotes the state of the mth of M chains at iteration n of N. Letting $\psi_{mn} \triangleq \psi(\theta_{mn})$, $\hat{R}$ is defined as follows:

$$\bar{\psi}_{m\cdot} \triangleq \frac{1}{N}\sum_{n}\psi_{mn}; \quad \bar{\psi}_{\cdot\cdot} \triangleq \frac{1}{MN}\sum_{m,n}\psi_{mn}; \tag{5}$$

$$\frac{B}{N} \triangleq \frac{1}{M-1}\sum_{m}(\bar{\psi}_{m\cdot} - \bar{\psi}_{\cdot\cdot})^2; \tag{6}$$

$$W \triangleq \frac{1}{M(N-1)}\sum_{m,n}(\psi_{mn} - \bar{\psi}_{m\cdot})^2; \tag{7}$$

$$\hat{\sigma}_{+}^2 \triangleq \frac{N-1}{N}W + \frac{B}{N}; \tag{8}$$

$$\hat{R} \triangleq \frac{M+1}{M}\frac{\hat{\sigma}_{+}^2}{W} - \frac{N-1}{MN}. \tag{9}$$

If the chains were initialized from their stationary distribution, then $\hat{\sigma}_{+}^2$ would be an unbiased estimate of the stationary distribution's variance. W is an estimate of the average within-chain variance; if the chains are stuck in isolated regions, then W should be smaller than $\hat{\sigma}_{+}^2$, and $\hat{R}$ will be clearly larger than 1. The $\frac{M+1}{M}$ and $\frac{N-1}{MN}$ terms are there to account for sampling variability—they vanish as N gets large if W approaches $\hat{\sigma}_{+}^2$.

Since $\hat{R}$ is defined in terms of a function of interest ψ, we can compute it for many such functions. In Section 5.1 we evaluated it for each weight and each predicted softmax probability in the test set.

C. Marginal distributions of the weights

In Section 4.1, we argued for using a trajectory length $\tau = \frac{\pi\sigma_{\text{prior}}}{2}$ based on the intuition that the posterior scale is determined primarily by the prior scale. In Figure 11 we examine this intuition. For each parameter, we estimate the marginal standard deviation of that parameter under the distribution sampled by HMC. Most of these marginal scales are close to the prior scale, and only a few are significantly larger (note logarithmic scale on y-axis), confirming that the posterior's scale is determined by the prior.

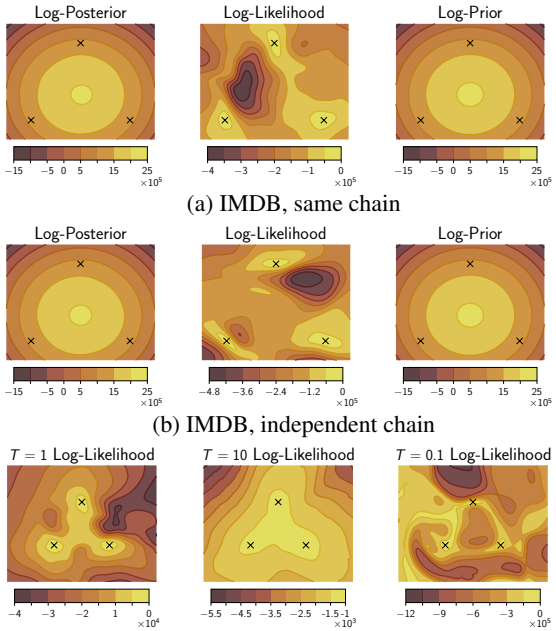

(a) IMDB, same chain

(b) IMDB, independent chain

(c) IMDB, Log-Likelihood at different T

Figure 12. **Additional posterior density visualizations.** Visualizations of posterior log-density, log-likelihood and log-prior in two-dimensional subspaces of the parameter space spanned by three HMC samples on IMDB using CNN-LSTM. **(a):** samples from the same chain and **(b)**: independent chains; **(c):** Log-likelihood surfaces for samples from the same chain at posterior temperatures $T = 1$, 10 and 0.1.

D. Additional Posterior Visualizations

In Section 5.2 we study two-dimensional cross-sections of posterior log-density, log-likelihood and log-prior surfaces. We provide additional visualizations on the IMDB dataset in Figure 12.

On IMDB, the posterior log-density is dominated by the prior, and the corresponding panels are virtually indistinguishable in Figure 12. For the CNN-LSTM on IMDB the number of parameters is much larger than the number of data points, and hence the scale of the prior density values is much larger than the scale of the likelihood. Note that the likelihood still affects the posterior typical set, and the HMC samples land in the modes of the likelihood in the visualization. In contrast, on ResNet-20, the number of parameters is smaller and the number of data points is larger, so the

posterior is dominated by the likelihood in Figure 3. The log-likelihood panels for both datasets show that HMC is able to navigate complex geometry: the samples fall in three isolated modes in our two-dimensional cross-sections. On IMDB, the visualizations for samples from a single chain and for samples from three independent chains are qualitatively quite similar, hinting at better parameter-space mixing compared to CIFAR-10 (see Section 5.1).

In Figure 12 (c), we visualize the likelihood cross-sections using our runs with varying posterior temperature on IMDB. The visualizations show that, as expected, low temperature leads to a sharp likelihood, while the high-temperature likelihood appear soft. In particular, the scale of the lowest likelihood values at $T = 10$ is only 10^3 while the scale at $T = 0.1$ is 10^6.

How are the visualizations created? To create the visualizations we pick the points in the parameter space corresponding to three HMC samples: w_1, w_2, w_3. We construct a basis in the 2-dimensional affine subspace passing through these three points: $u = w_2 - w_1$ and $v = w_3 - w_1$. We then orthogonalize the basis: $\hat{u} = u/\|u\|$, $\hat{v} = (v - \hat{u}^T v)/\|v - \hat{u}^T v\|$. We construct a 2-dimensional uniform grid in the basis $\hat{u}, \hat{v}$. Each point in the grid corresponds to a vector of parameters of the network. We evaluate the log-likelihood, log-prior and posterior log-density for each of the points in the grid, converting them to the corresponding network parameters. Finally, we produce contour plots using the collected values. The procedure is analogous to that used by Garipov et al. (2018)[6].

E. HMC Predictive Distributions in Synthetic Regression

We consider a one-dimensional synthetic regression problem. We follow the general setup of Izmailov et al. (2019) and Wilson & Izmailov (2020). We generate the training inputs as a uniform grid with 40 points in each of the following intervals (120 datapoints in total): $[-10, -6]$, $[6, 10]$ and $[14, 18]$. We construct the ground truth target values using a neural network with 3 hidden layers, each of dimension 100, one output and two inputs: following Izmailov et al. (2019), for each datapoint x we pass x and x^2 as inputs to the network to enlarge the class of functions that the network can represent. We draw the parameters of the network from a Gaussian distribution with mean 0 and standard deviation 0.1. We show the sample function used to generate the target values as a black line in each of the panels in Figure 13. We then add Gaussian noise with mean 0 and standard deviation 0.02 to each of the target values. The final dataset used in the experiment is shown with red circles in Figure 13.

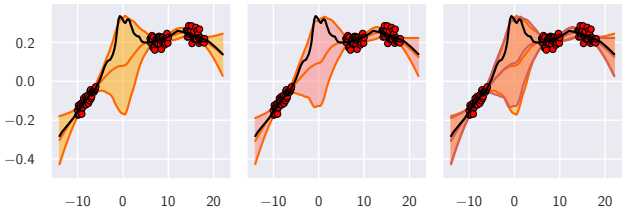

(a) Chain 1 (b) Chain 2 (c) Overlaid

Figure 13. **HMC chains on synthetic regression.** We visualize the predictive distributions for two independent HMC chains on a synthetic regression problem with a fully-connected network. The data is shown with red circles, and the true data generating function is shown with a black line. The shaded region shows 3 standard deviations of the predictive distribution, and the predictive mean is shown with a line of the same color. In panels **(a)**, **(b)** we show the predictive distributions for each of the two chains individually, and in panel **(c)** we overlay them on top of each other. The chains provide almost identical predictions, suggesting that HMC mixes well in the prediction space.

For inference, we use the same model architecture that was used to generate the data. We sample the initialization parameters of the network from a Gaussian distribution with mean 0 and standard deviation 0.005. We use a Gaussian distribution with mean zero and standard deviation 0.1 as the prior over the parameters, same as the distribution used to sample the parameters of the ground truth solution. We use a Gaussian likelihood with standard deviation 0.02, same as the noise distribution in the data. We run two HMC chains from different random initializations. Each chain uses a step-size of 10^{-5} and the trajectory length is set according to the strategy described in Section 4.1, resulting in 15708 leapfrog steps per HMC iteration. We run each chain for 100 HMC iterations and collect the predictions corresponding to all the accepted samples, resulting in 89 and 82 samples for the first and second chain respectively. We discard the first samples and only use the last 70 samples from each chain. For each input point we compute the mean and standard deviation of the predictions.

We report the results in Figure 13. In panels (a), (b) we show the predictive distributions for each of the chains, and in panel (c) we show them overlaid on top of each other. Both chains provide high uncertainty away from the data, and low uncertainty near the data as desired (Yao et al., 2019). Moreover, the true data-generating function lies in the 3σ-region of the predictive distribution for each chain. Finally, the predictive distributions for the two chains are almost identical. This result suggests that on the synthetic problem under consideration HMC is able to mix in the space of predictions, and provides similar results independent of initialization and random seed. We come to the same conclusion for more realistic problems in Section 5.

[6] See also the blogpost https://izmailovpavel.github.io/curves_blogpost/, Section "How to Visualize Loss Surfaces?".

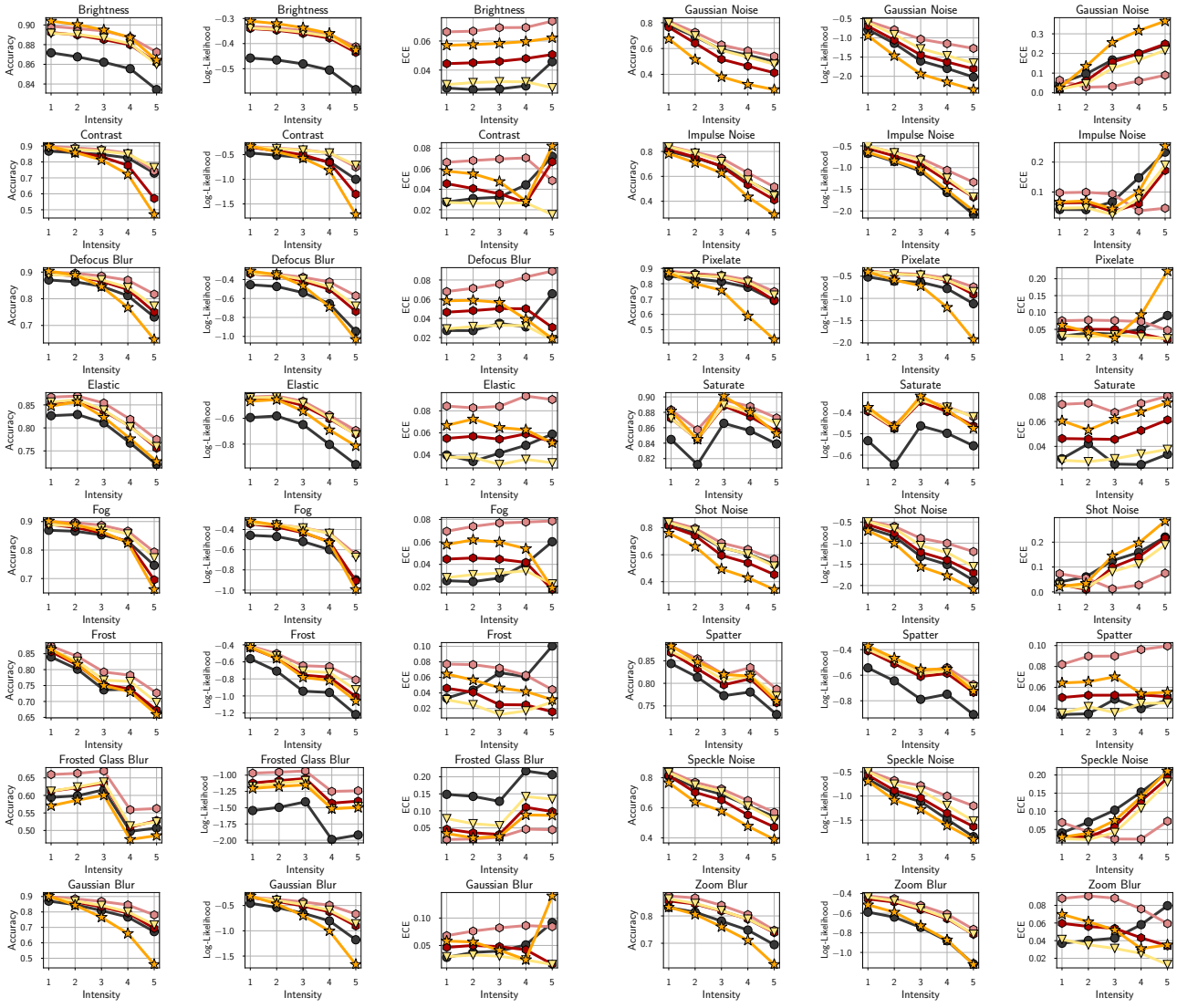

Figure 14. **Performance under corruption.** We show accuracy, log-likelihood and ECE of HMC, SGD, Deep Ensembles, SGLD and SGHMC-CLR-Prec for all 16 CIFAR-10-C corruptions as a function of corruption intensity. HMC shows poor accuracy on most of the corruptions with a few exceptions. SGLD provides the best robustness on average.

F. BNNs are not Robust to Domain Shift

In Section 6.2, Figure 7 we have seen that surprisingly BNNs via HMC underperform significantly on corrupted data from CIFAR-10-C compared to SGLD, deep ensembles and even MFVI and SGD. We provide detailed results in Figure 14. HMC shows surprisingly poor robustness in terms of accuracy and log-likelihood across the corruptions. The ECE results are mixed. In most cases, the HMC ensemble of 720 models loses to a single SGD solution!

The poor performance of HMC on OOD data is surprising. Bayesian methods average the predictions over multiple models for the data, and faithfully represent uncertainty. Hence, Bayesian deep learning methods are expected to be robust to noise in the data, and are often explicitly evaluated on CIFAR-10-C (e.g. Wilson & Izmailov, 2020; Dusenberry et al., 2020). Our results suggest that the improvements achieved by Bayesian methods on corrupted data may be a sign of *poor* posterior approximation.

To further understand the robustness results, we reproduce the same effect on a small fully-connected network with two hidden layers of width 256 on MNIST. We run HMC at temperatures $T = 1$ and $T = 10^{-3}$ and SGD and report the results for both the BMA ensembles and individual samples in Figure 15. For all methods, we train the models on the original MNIST training set, and evaluate on the test set with random Gaussian noise $\mathcal{N}(0, \sigma^2 I)$ of varying scale σ. We report the test accuracy as a function of σ. We find that while the performance on the original test set is very close for all methods, the accuracy of HMC at $T = 1$ drops much quicker compared to that of SGD as we increase the noise scale.

Notably, the individual sample performance of $T = 1$ HMC is especially poor compared to SGD. For example, at noise scale $\sigma = 3$ the SGD accuracy is near 60% while the HMC sample only achieves around 20% accuracy!

HMC can be though of as sampling points at a certain sub-optimal level of the training loss, significantly lower than that of SGD solutions. As a result, HMC samples are individually inferior to SGD solutions. On the original test data ensembling the HMC samples leads to strong performance significantly outperforming SGD (see Section 6). However, as we apply noise to the test data, ensembling can no longer close the gap to the SGD solutions. To provide evidence for this explanation, we run evaluate HMC at a very low temperature $T = 10^{-3}$, as low temperature posteriors concentrate on high-performance solutions similar to the ones found by SGD. We find that at this temperature, HMC performs comparably with SGD, closing the gap in robustness We have also experimented with varying the prior scale but were unable to close the gap in robustness at temperature $T = 1$.

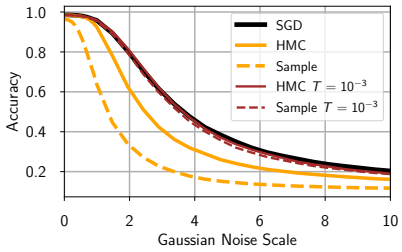

Figure 15. **Robustness on MNIST.** Performance of SGD, BMA ensembles and individual samples constructed by HMC at temperatures $T = 1$ and $T = 10^{-3}$ on the MNIST test set corrupted by Gaussian noise. We use a fully-connected network. Temperature 1 HMC shows very poor robustness, while lowering the temperature allows us to close the gap to SGD.

We hypothesize that using a lower temperature with HMC would also significantly improve robustness on CIFAR-10-C. Verifying this hypothesis, and generally understanding the robustness of BNNs further is an exciting direction of future work.

G. Further discussion of cold posteriors

In Section 7 we have seen that the cold posteriors are not needed to achieve strong performance with BNNs. We have even shown that cold (as well as warm) posteriors may hurt the performance. On the other hand, in Appendix F we have shown that lowering the temperature can improve robustness under the distribution shift, at least for a small MLP on MNIST. Here, we discuss the potential reasons for why the cold posteriors effect was observed in Wenzel et al. (2020).

G.1. What causes the difference with Wenzel et al. (2020)?

There are several key differences between the experiments in our study and Wenzel et al. (2020).

First of all, the predictive distributions of SGLD (a version of which was used in Wenzel et al. (2020)) are highly dependent on the hyper-parameters such as the batch size and learning rate, and are inherently biased: SGLD with a non-vanishing step size samples from a perturbed version of the posterior, both because it omits a Metropolis-Hastings accept-reject step and because its updates include minibatch noise. Both of these perturbations should tend to make the entropy of SGLD's stationary distribution increase with its step size; we might expect this to translate to approximations to the BMA that are overdispersed.

Furthermore, Wenzel et al. (2020) show in Figure 6 that with a high batch size they achieve good performance at $T = 1$ for the CNN-LSTM. Using the code provided by the

	ACC, $T = 1$	ACC, $T = 0.1$	CE, $T = 1$	CE, $T = 0.1$
BN + AUG	87.46	91.12	0.376	0.2818
FRN + AUG	85.47	89.63	0.4337	0.317
BN + NO AUG	86.93	85.20	0.4006	0.4793
FRN + NO AUG	84.27	80.84	0.4708	0.5739

Table 7. **Role of data augmentation in the cold posterior effect.** Results of a single chain ensemble constructed with the SGHMC-CLR-Prec sampler of Wenzel et al. (2020) at temperatures $T = 1$ and $T = 0.1$ for different combinations of batch normalization (BN) or filter response normalization (FRN) and data augmentation (Aug). We use the ResNet-20 architecture on CIFAR-10. Regardless of the normalization technique, the cold posteriors effect is present when data augmentation is used, and not present otherwise.

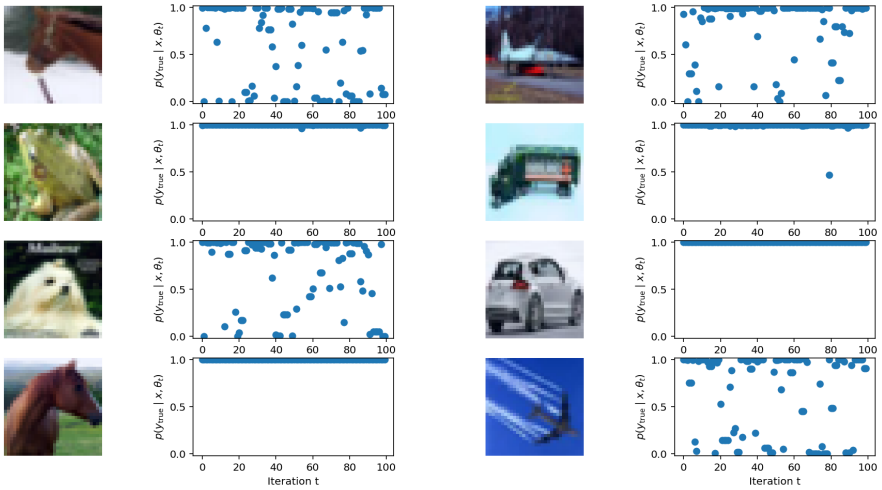

Figure 16. **HMC samples are (over)confident classifiers.** Plots show the probability assigned by a series of HMC samples to the true label of a held-out CIFAR-10 image. In many cases these probabilities are overconfident (i.e., assign the right answer probability near 0), but there are always *some* samples that assign the true label high probability, so the Bayesian model average is both accurate and well calibrated. These samples were generated with a spherical Gaussian prior with variance $\frac{1}{5}$.

autors[7] with default hyper-parameters we achieved strong performance at $T = 1$ for the CNN-LSTM (accuracy of 0.855 and cross-entropy of 0.35, compared to 0.81 and 0.45 reported in Figure 1 of Wenzel et al. (2020)); we were, however, able to reproduce the cold posteriors effect on CIFAR-10 using the same code.

On CIFAR-10, the main difference between our setup and the configuration in Wenzel et al. (2020) is the use of batch normalization and data augmentation. In the appendix K and Figure 28 of Wenzel et al. (2020), the authors show that if both the data augmentation and batch normalization are turned off, we no longer observe the cold posteriors effect. In Table 7 we confirm using the code provided by the authors that in fact it is sufficient to turn off just the data augmentation to remove the cold posteriors effect. It is thus likely that the results in Wenzel et al. (2020) are at least partly affected by the use of data augmentation.

[7] https://github.com/google-research/google-research/tree/master/cold_posterior_bnn

H. Visualizing prediction variations in HMC samples

In Figure 16 we visualize the predicted class probability of the true class for 100 HMC samples on eight different input images. While on some images the predicted class probability is always close to 1, on other inputs it is close to 1 for some of the samples (confidently correct), close to 0 for some of the samples (confidently wrong) and in between 0 and 1 for the remaining samples (unconfident). So, some of the samples are individually over-confident, but the ensemble is well-calibrated as other samples assign high probabilities to the correct class.